The Thesis Committee for Stephen Boyer Graf
Certifies that this is the approved version of the following thesis

Pore fluid pressure detection within the plate boundary fault interface of the Costa Rica convergent margin using AVO attributes

APPROVED BY

SUPERVISING COMMITTEE:

Supervisor: Nathan Bangs

Co-Supervisor: Kirk McIntosh

Robert Tatham

Mark Cloos

Pore fluid pressure detection within the plate boundary fault interface of the Costa Rica convergent margin using AVO attributes

by

Stephen Boyer Graf, BSGeoSci

Thesis

Presented to the Faculty of the Graduate School of

The University of Texas at Austin

in Partial Fulfillment

of the Requirements

for the Degree of

Master of Science in Geological Sciences

The University of Texas at Austin

December 2012

Dedication

In memory of Kathryn Elizabeth Boyer Vine

Acknowledgments

The author would like to thank his supervisors, Dr. Nathan Bangs and Dr. Kirk McIntosh, for the opportunity to work on the Costa Rica Seismogenesis Project 3D seismic reflection survey. The ability to assist in acquiring, processing, and interpreting the data was an invaluable learning experience, and their guidance and support was critical throughout all stages of my project. Committee members, Dr. Robert Tatham and Dr. Mark Cloos, provided perspectives on geophysical seismic attributes and geologic principles of subduction zones that enhanced the author's education. Additionally, the task of thoroughly processing the 3D seismic volume could not have been done without the advice of Thomas Hess and computer support of Mark Wiederspahn. Without generous support from the National Science Foundation, the University of Texas Institute for Geophysics, and the Jackson School of Geosciences, the work presented below would not have been possible.

Family members Kermit and Sandra Graf, Christopher and Robyn Graf, and Ryan and Erin Graf were extremely gracious and supportive, and I cannot thank them enough.

Lastly, the author would also like to express his deep gratitude and appreciation towards his wife, Jennifer, whose love and encouragement was pivotal from beginning to end.

Abstract

Pore fluid pressure detection within the plate boundary fault interface of the Costa Rica convergent margin using AVO attributes

Stephen Boyer Graf, MSGeoSci

The University of Texas at Austin, 2012

Supervisors: Nathan Bangs and Kirk McIntosh

I conducted an amplitude vs. offset (AVO) analysis on newly acquired 3D seismic reflection data to detect elevated pore fluid content and pore fluid pressure along the Costa Rica convergent margin to address dewatering processes of subduction zone sediments. These data provide the highest quality 3D seismic data acquired to date along a convergent margin for detailed analysis of geophysical properties along the plate boundary fault interface. In 2011, a 55 km by 11 km 3D seismic reflection survey was completed using the *R/V Marcus G. Langseth* offshore western Costa Rica at the convergent margin of the Cocos and Caribbean plates. We applied pre-stack Kirchhoff time migration to a subset of these data across the frontal prism where amplitude versus offset (AVO) attributes were extracted along the decollement. When pore fluid pressure, λ^*, exceeds $\lambda^* \approx 0.7$, the pressure at which Poisson's ratio begins to approach that of water, the AVO response of a fluid-filled, clay-rich decollement requires a high Poisson's ratio and an excessively low seismic P-wave and S-wave velocity. Acute wedge taper, undercompacted subducted hemipelagic and pelagic sediments, and a smooth decollement in the northwest half of

the survey correspond with decollement AVO response of relatively high values of Poisson's ratio. These findings suggest increased pore fluid content and vertical containment of near-lithostatic pore fluid pressures within the decollement. In contrast, increased wedge taper angles, thin hemipelagic and pelagic sediments, and a rugose decollement beneath the southeastern frontal prism produce an AVO response interpreted as due to lower pore fluid contents and pressures. We propose that large-offset subducting basement normal faults in this area, as close as 20 m from the decollement, induce vertical fractures within the decollement that allow for fluid expulsion into the frontal prism and lower fluid pressure. Lateral variability of overpressure within the decollement shear zone of subduction margins is important in understanding the evolution of frontal prism strain accumulation and seismogenic rupture.

Table of Contents

List of Figures

Chapter 1: Introduction

1.1 PROBLEM

Previous studies of the plate boundary fault interface between the subducting Cocos plate and overlying Caribbean plate offshore western Costa Rica have focused largely on initial dewatering of subducting, fluid-rich hemipelagic and pelagic clays beneath the frontal prism. For the first time, industry-quality, high-resolution 3D seismic data is suitable for the extraction of advanced geophysical attributes in order to view fault zone properties across a broad 10×15 km area of a subduction zone thrust plane. Specifically, amplitude versus offset (AVO) attributes are used to assess relative changes in Poisson's ratio along the plate interface where fractured, brine-saturated hemipelagic sediments are thrust beneath deformed and accreted clays (Shipley et al., 1992). AVO analysis techniques exploit the variation in seismic P-wave reflection amplitudes with angle of incidence at the reflecting surface to estimate the contrast in elastic parameters across the reflection interface.

Fluids within the plate boundary interface of subduction zones are held within fractures, intergranular pore space, and hydrous minerals (Saffer and Tobin, 2011). Along the Costa Rica margin, incoming hemipelagic and pelagic sediments undergo dewatering during initial subduction due to the increase of overburden stress leading to sediment compaction on the order of 20 - 50 % and fluid expulsion, likely along permeable normal faults or fractures (McIntosh and Sen, 2000). A high convergence rate of 93 mm/yr (DeMets et al., 1994) and low permeability of subducting sediments on the order of $10^{-14}k$ (Saffer and Tobin, 2011), however, provides the likelihood for subducted sediments beneath the frontal prism to be undercompacted for the depth of burial and lead to overpressured con-

ditions where the pore fluid pressure is greater than hydrostatic pressure (Saffer and Tobin, 2011). Any localized areas of high fluid content observed seismically is likely due to undercompaction and may lead to high pore fluid pressures that preserve porosity. Areas of lower fluid content are likely under higher effective normal stress than are areas with high fluid content, creating conditions suitable for high strain accumulations along the decollement. By identifying overpressure localities along the frontal prism decollement, we may then map lateral strain accumulation variation and view where the frontal prism may be preferentially locked or unlocked. Ide et al. (2011) suggest a link between frontal prism displacement and tsunami genesis during the 2011 M_w 9.0 Tohoku-Oki earthquake, indicating the potential for strain accumulation and release near the trench.

The exact processes that facilitate dewatering of subducted sediments within the frontal prism of subduction margins is still relatively unknown. Here I look at local fluid content and fluid pressure heterogeneities within the decollement in an effort to not only quantify pore fluid pressures, but also to propose mechanisms for decollement dewatering during the initial stages of subduction within 5 km of the trench axis. Understanding local pressure and fluid content heterogeneities from seismic data is difficult, yet the convergent margin offshore Costa Rica provides a unique opportunity to view these features in more detail than ever before. The relationship between pressures and fluids along the decollement in the aseismic area are the updip components that feed directly into the seismogenic zone farther downdip. High fluid quantities are carried downdip as subduction continues and, along with quartz precipitation and low temperature mineral phase alteration (Saffer and Marone, 2003), may influence elastic strain accumulation and the depth of the seismogenic zone.

1.2 OVERVIEW

The Costa Rica subduction margin constitutes smooth subduction with low seafloor topography to the northwest near the Nicoya peninsula, subducting seamounts between the Nicoya and Osa peninsulas, and subduction of the Cocos Ridge offshore of the Osa peninsula. The Costa Rica Seismogenesis Project (CRISP) 3D seismic survey is located offshore western Costa Rica to the northwest of the Osa peninsula and in an area containing no current seamount subduction (Figure 1.1). Incipient subduction of the Costa Rica margin occurred during the late Campanian (Buchs et al., 2010) and flat slab subduction is a likely cause of northeast migration of the volcanic arc during the last 50 Ma (Lissinna et al., 2002). The Costa Rica subduction zone is largely identified as an erosional margin because conditions here include low sediment supply, high rate of subduction, and the presence of subducting seafloor topography, all of which aid the process of subduction erosion (von Huene, 1986).

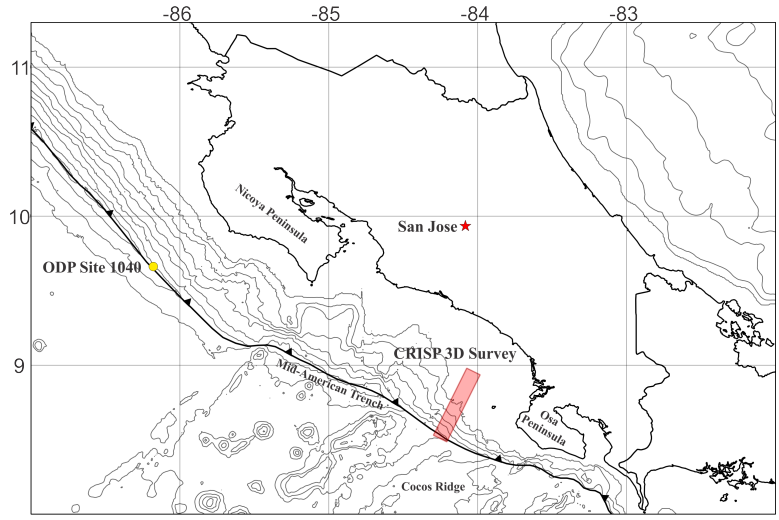

Figure 1.1: Map of the Middle America Trench offshore western Costa Rica. The Costa Rica Seismogenesis Project (CRISP) 3D seismic survey is highlighted in red. Ocean Drilling Program (ODP) leg 170, site 1040 borehole location is highlighted in yellow.

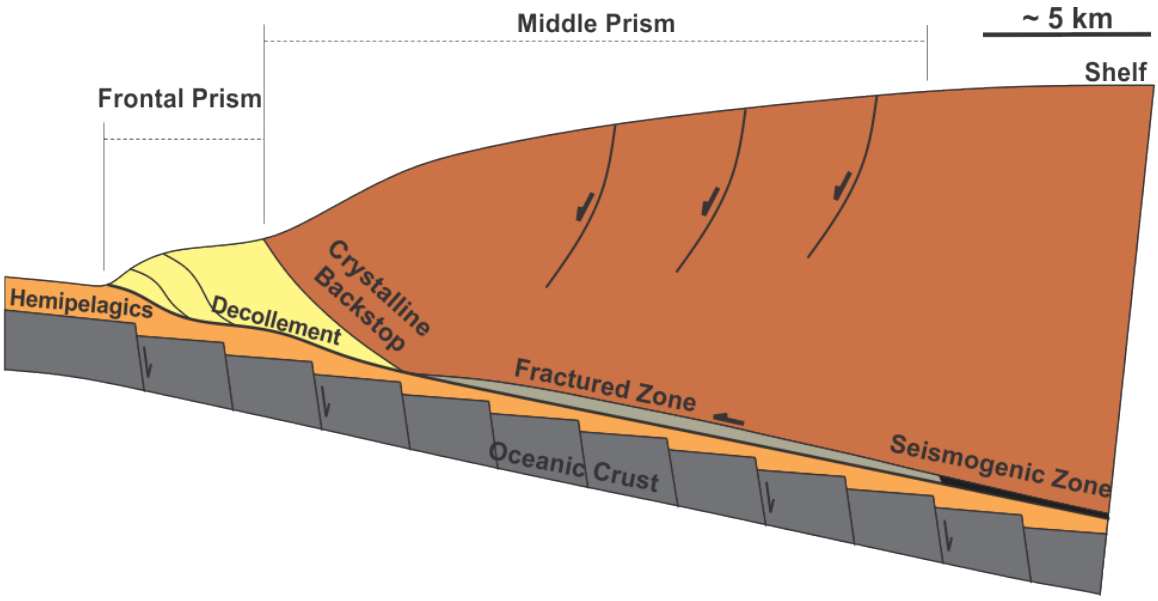

Figure 1.2: Generalized model of the Costa Rican margin adapted from Wang et al. (2010) and von Huene et al. (2004). The frontal prism, comprised of structurally deformed clays, is seaward of a crystalline backstop. Underthrust hemipelagic and pelagic sediments overlay normally faulted oceanic basement. Downdip from the frontal prism, the plate boundary fault interface is proposed by von Huene et al. (2004) to be highly fractured, allowing for material to be eroded off the overlying middle prism and carried downdip eventually into the seismogenic zone. Extensional faulting is seen in the middle prism, perhaps caused by erosion along the base of the margin.

Primary features of a subduction margin include the overlying wedge, subducting oceanic crust, and the plate boundary interface. For the Costa Rica margin, the overlying wedge may be broken down further into a structurally deformed, frontally accreted frontal prism, and a crystalline middle prism (Figure 1.2) (von Huene et al., 2004). Much of the stress and strain accommodation within the frontal prism is along the decollement fault interface where the prism is assumed to be in a compressively critical state of failure over large time scales (Davis et al., 1983; Wang and Hu, 2006).

Here, the decollement is defined as a subparallel detachment fault relative to the oceanic crust that splays upward from subducting oceanic crust, propagates updip, and

terminates at, or near, the trench. In the subduction zone offshore western Costa Rica, material above the decollement in the frontal prism is the deformed sediment wedge composed mainly of very fine-grained sediments and clays. The underthrust material is green, fractured, hemipelagic, silty clay of Pleistocene age that overlays white, carbonate, pelagic sediments of Miocene age (Tobin et al., 2001). Such lithologic partitioning between the frontal prism and the underthrust sediment allows for increases in fluid content due to undercompaction that may result in buildup of overpressure within the decollement. High pore pressure along a fault plane decreases the effective normal stress along that plane and allows for preferential movement along the fault (Tobin et al., 2001). Tobin et al. (2001) also note that the decollement zone offshore the Nicoya peninsula at ODP site 1070 was itself partitioned into a ductile lower zone and a fractured upper zone where active fluid flow occurs at a rate on the order of $8\,m^3 \cdot yr^{-1}$ (Saffer et al., 2000). The premise of a fractured upper decollement beneath the frontal prism is key because this idea allows fluid content heterogeneity that may then be detected with advanced geophysical analysis techniques.

Figure 1.3 is a southwest- to northeast-trending, dip-oriented seismic profile perpendicular to the trench axis taken from the CRISP 3D dataset. It outlines the seafloor, decollement, basement, and hemipelagic reflecting horizons. The decollement is mapped as a negative amplitude reflection event within the frontal prism, below which is compacted hemipelagic sediments above oceanic crust that exhibits pervasive normal faulting.

A fluid-rich decollement zone, with porosities near 70% proximal to the trench axis (Davis and Villinger, 2006), underlies the deformed frontal prism and will produce a negative reflection coefficient because the velocity and density of the decollement is less than the overlying prism (Figure 1.4). Compared to normally compacted underthrust sediments, areas along the decollement that are undercompacted will have higher fluid content and pore pressure, causing the formation velocity to decrease, creating an even stronger

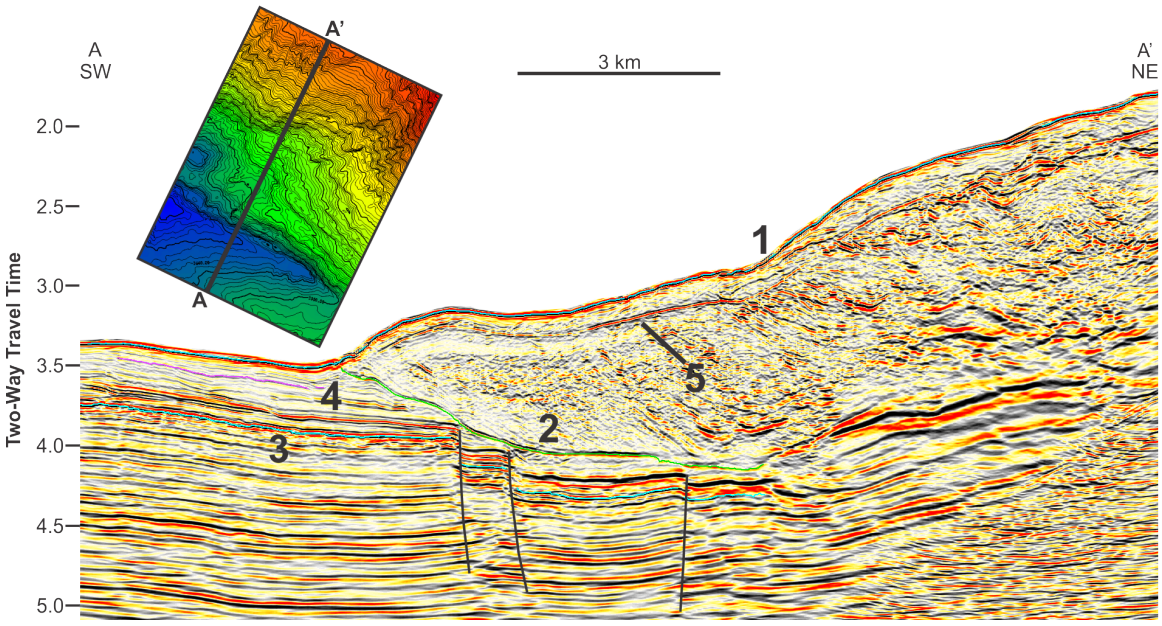

Figure 1.3: Dip-oriented profile A illustrates 1) the mapped seafloor horizon, 2) the negative amplitude decollement, 3) subducting oceanic basement exhibiting normal faulting, 4) a reflection mapped within the hemipelagic sedimentary section, 5) negative reflection bottom-simulating reflector (BSR).

negative reflection event. Decollement reflection amplitude response of common midpoint (CMP) stacked data may provide a good first order approximation of where high fluid content may exist, but other variables also contribute to seismic response such as changes in lithology, grain size, and porosity. Amplitude versus offset (AVO) techniques allow for analysis in finer detail because they are closely related to Poisson's ratio, the ratio between lateral and longitudinal strain (Ostrander, 1984). Increases in fluid content will effectively increase Poisson's ratio within the decollement enough for AVO attribute detection. A "soft" water bottom, thin frontal wedge, and industry-quality seismic data provide sufficient source-receiver offset and signal-to-noise ratio in the seismic response so that AVO analysis of 3D seismic data may be successfully applied to quantify pore fluid pressures from inferred changes in the dynamic Poisson's ratio across the entire decollement reflec-

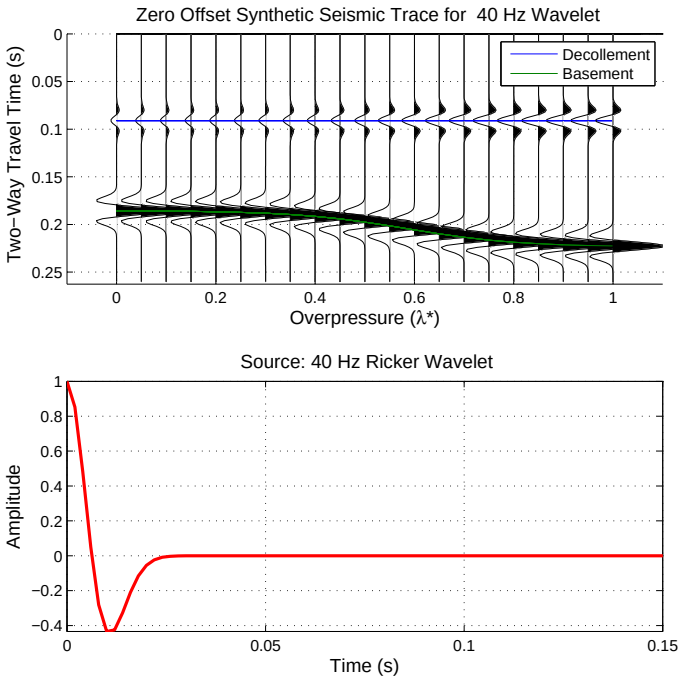

Figure 1.4: The top plot shows the zero-offset synthetic seismic reflection traces over all pore pressure scenarios. λ^* is the fractional value of overpressure between hydrostatic ($\lambda^* = 0$) and lithostatic ($\lambda^* - 1$) pressure. The decollement is a negative amplitude event due to a decrease in the product of velocity and density across the interface. Increases in pore fluid pressure decrease the velocity beneath the decollement, creating a stronger, negative event at high pore fluid pressures. The bottom plot shows the 40 Hz Ricker wavelet used to create the synthetic seismogram.

tion surface. Areas with low fluid content and pore pressure along the decollement may indicate increased basal friction, allowing for strain accumulation, and may be prone to displacement during the next earthquake cycle.

1.3 ADVANCEMENTS

For the first time, the 3D seismic reflection survey acquired offshore Costa Rica provides a unique opportunity to apply AVO analysis to quantify the fluid content and

pore fluid pressures within the decollement. Given sufficient seismic data quality, 3D AVO techniques are an effective tool in shallow subduction settings to estimate changes in specific elastic parameters used to identify spatial variation in pore fluid content and pressure within decollement. Prasad (2002) shows that laboratory seismic velocity estimations on unlithified fine-to medium-grained sand decrease as a power-law function of increasing pore fluid pressure. Application of AVO techniques in a clay-rich, undercompacted, and fractured environment, however, yields an AVO response that cannot be explained by a power-law velocity-pore pressure relationship. Therefore, I propose a modified velocity relationship as a logistic function of pore pressure that effectively lowers the rate of velocity decrease at near-lithostatic pore pressures (Figure 1.5). This causes the seismic P-wave velocity to asymptotically approach a minimum value as lithostatic pore pressures are reached. Further, AVO analysis within the decollement suggests lateral variation in pore fluid pressure which I, in turn, can relate in part to variation in structure of the subducting oceanic plate and overlying frontal prism.

Within the 3D survey area of the frontal prism, the decollement exhibits two distinct areas with specific seismic characteristics: a smooth, well-imaged reflector in the northwest area of the survey, and a rugose, poorly imaged reflector toward the southeast. The AVO analysis of the well-imaged area is consistent with increased pore fluid pressure relative to hydrostatic pore pressures measured seaward of the trench axis. This area contains trench-perpendicular bands of high fluid content that are interpreted to be areas of high fluid pressure and, consequently, low basal friction. This result is corroborated with low wedge taper angles of the frontal prism and underthrust hemipelagic sediments $\approx$ 300 m to 400 m thick, thereby pointing to an undercompacted, fluid-rich decollement with low basal friction that is able to accommodate up to 6 km of slip over approximately 65,000 years. The locally high pore pressure here is a result of low permeability and un-

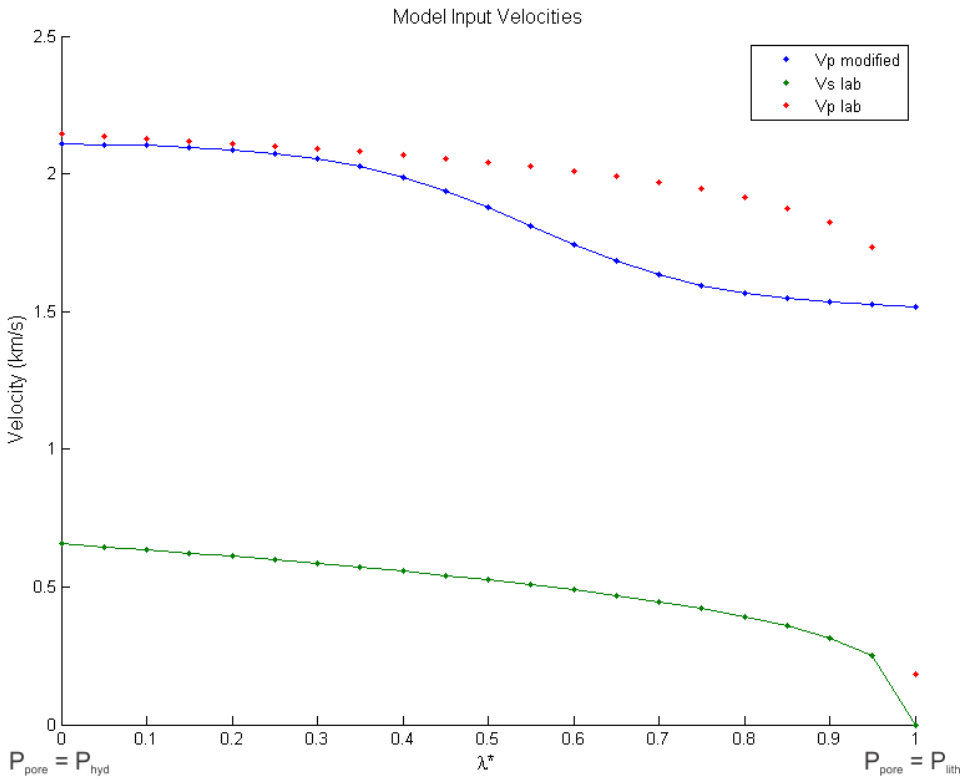

Figure 1.5: Modified velocity functions for V_p and V_s. V_s is the same trend from the Prasad (2002) laboratory data, but the V_p curve has been modified to fit a logistic function that begins to reach a lower limit at high overpressures. At $\lambda^* = 0$, the pore fluid pressure, P_{pore}, equals the hydrostatic pressure, P_{hyd}. When $\lambda^* = 1$, P_{pore} equals the overburden lithostatic pressure, P_{lith}.

dercompacted hemipelagic clays that are able to contain elevated pore pressures to within the decollement plate boundary fault interface.

Lower estimates of Poisson's ratio in the southeast area of the decollement is consistent with lower pore fluid content relative to the northwest area. Low fluid content may be associated with lower pore fluid pressures than are observed towards the northwest, causing the normal effective stress to increase, leading to higher basal friction values. Such areas of high basal friction correspond to increased wedge taper angles and thinner

($\approx$ 50 m to 150 m) underthrust sediments in the southeast, leading to increased strain accumulation and expulsion of fluids from a compacted decollement. High reflection amplitude reflections from the decollement in this area occur on the upthrown and downthrown side of basement normal faults that actively influence the structure of the decollement. These fault-bound amplitude anomalies may indicate local, structurally-influenced pressure isolation. Large-offset basement normal faults in close proximity ($\approx$ 10 m to 20 m) to the decollement are proposed to induce vertical fractures within the decollement as the decollement conforms to the subducting topography. This then creates a pathway for upward migration of fluids away from the decollement and into the overlying frontal prism.

The Costa Rica 3D seismic survey reveals an area towards the northwest that exhibits low frontal prism taper angle, a smooth decollement beneath the frontal prism, and undercompacted hemipelagic sediments subducted beneath the prism. This is in stark contrast to the southeast area that shows overall larger frontal prism taper angles, a decollement that is heavily influenced by subducting normal faults, and thin hemipelagic sediments beneath the prism. With these observations and a modified seismic propagation velocity function, I propose that the northwest survey area is conducive to pressure containment within the decollement, whereas vertical fracturing of the decollement caused by subducting normal faults to the southeast provide a conduit for fluid expulsion away from the decollement. Pore fluid pressure conditions in the southeast lead to increased basal friction and strain accumulation within the frontal prism.

1.4 Organization of Thesis

Chapter 2 will discuss the geologic setting of the Costa Rica margin and why it provides an excellent setting for 3D seismic data acquisition. Previous studies about pore pressure development and erosional processes along the Costa Rica margin provide key

background knowledge and input conditions for needed modeling. Model variables detailed in Chapter 3 include estimates of pore pressure, bulk density, and P- and S-wave velocities of the overlying frontal prism and underlying decollement.

CRISP 3D seismic reflection survey acquisition parameters outlined in Chapter 3 allow for AVO analysis on high-resolution data to be performed for the first time on a convergent margin. The 3D seismic data set allows for calculation of normal incidence reflectivity, A, and amplitude gradient, B, from pre-stack, time migrated, common midpoint gathers and are used to approximate subsurface conditions along the decollement. Comparison between results from modeling and seismic data requires a unifying set of assumptions on velocity and density that are elaborated upon in Chapter 3.

Chapter 4 presents structural observations of the frontal prism and presents the AVO response disparity between the modeled decollement and the decollement from the 3D seismic data. My interpretation of the observations is discussed in detail in Chapter 5, where I propose explanations to the AVO disparity and the structural differences within the frontal prism. I then present the conclusions of this study in Chapter 6 regarding the link between induced fractures, pore fluid pressures, and the structure of the frontal prism.

Chapter 2: Background

2.1 Geologic Setting

The Cocos plate subducts beneath the Caribbean plate near the Osa peninsula at 93 mm/yr (DeMets et al., 1994) as part of the Costa Rica subduction margin offshore western Costa Rica that results in active seismicity along the margin. The Costa Rica margin is characterized by a smooth subducting plate off the Nicoya peninsula, pervasive seamount subduction southwest of the Nicoya peninsula, and subduction of the Cocos Ridge off of the Osa peninsula that began as early as 5 Ma (Meschede et al., 1999; von Huene et al., 2000) or as recently 0.5 Ma (Morell et al., 2012). Often cited as an erosional margin (von Huene et al., 2000; Ranero and von Huene, 2000; von Huene et al., 2004), the Costa Rica margin possesses a high rate of subduction and low sediment supply that helps the process of subduction erosion (von Huene, 1986). Tectonic erosion offshore Costa Rica is currently proposed to occur by high pore fluid pressures fracturing portions of the overlying plate, allowing the subducting oceanic basement to carry fragmented rock from the upper plate into the shear zone and farther downdip (von Huene et al., 2004). Erosion of material from the underside of the overriding plate is expressed by pervasive extensional normal faulting (Figure 2.1) into the inner wedge (von Huene et al., 2004; Wang et al., 2010). Shipley et al. (1992), however, observed underplating and accretion of subducted sediments to the overriding plate within the frontal prism. Therefore, an overall erosional margin may exhibit accretionary features within the frontal prism.

As subduction occurs, increased shear stress along the plate boundary interface accumulates elastic strain that may be released seismically as discrete seismogenic ruptures, or high stresses may not accumulate and lead to smooth, aseismic subduction. Figure 2.2

identifies the region of aseismic slip behavior beneath the overriding frontal prism near the trench. Conditionally stable seismic asperities serve as a transition zone farther downdip and is where tremors and low frequency earthquakes (LFE) originate (Saffer and Tobin, 2011). Finally, the seismically unstable region known as the seismogenic zone is an area where seismic rupture nucleates and propagates updip, downdip, and laterally across the fault interface (Scholz, 1998; Bilek and Lay, 2002). Figure 2.2 illustrates an accretionary prism where sediment accumulation on the overlying wedge is greater than the sediment flux being subducted. These gross observations may also be applied to erosional margins. The focus of this study is located within the aseismic-stable region of Figure 2.2, where strain is accommodated aseismically (Bilek and Lay, 2002).

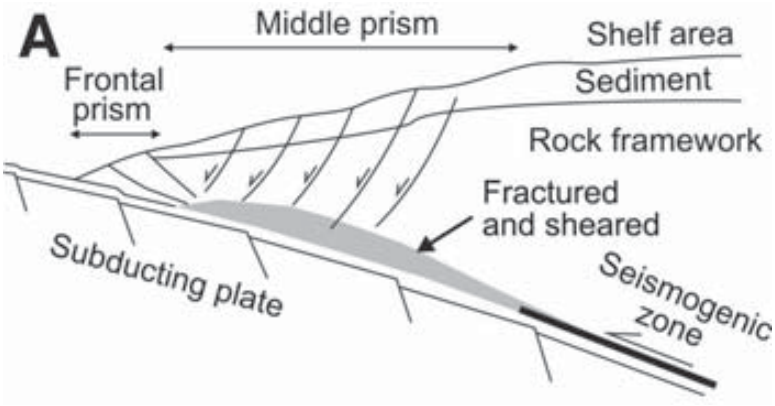

Figure 2.1: As material is eroded off the upper plate, the middle prism undergoes extension during interseismic periods (Wang et al., 2010).

Subducting seafloor topographic features and increased basal friction have been cited as key factors in subduction erosion where subducting seamounts may initiate high fault plane friction and become likely areas of earthquake nucleation (Ranero and von Huene, 2000). Recent studies along the Costa Rica margin, however, propose near lithostatic pore pressures and low basal friction along the plate boundary interface as a key

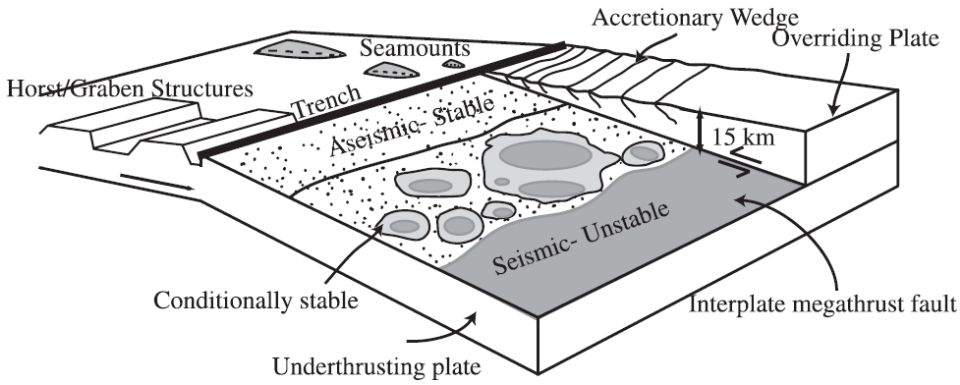

Figure 2.2: Subduction zone diagram from Bilek and Lay (2002). The transition from aseismic to seismic slip occurs downdip. This study is focused on detailed features within the aseismic-stable region.

factor in erosional margins (von Huene et al., 2004; Wang and Hu, 2006; Wang et al., 2010). In the low basal friction model, high pore fluid pressures effectively hydrofracture the underside of the overlying wedge where material is then broken off and carried into the subduction channel (von Huene et al., 2004). Knowledge of lateral fluid content variation along the decollement fault interface may provide insight into the pore pressure variation and amount of fluid in the frontal prism and is critical to understanding erosional processes downdip along the plate boundary interface.

Incoming fluid-filled sediments in a subduction margin appear to undergo substantial dewatering (between 20% and 60%) as they approach the thrust front of the margin (McIntosh and Sen, 2000, Saffer et al., 2000). Subsequent compaction appears to be minimal because high sediment loading rate, low permeability of the sediments, and relative lack of sufficient dewatering conduits, such as normal faults or stratigraphic conduits, inhibit further expulsion of fluid (Saffer and Tobin, 2011). In Costa Rica, dewatering within a few kilometers landward of the trench appears to be isolated to the upper hemipelagic sediments and little-to-no compaction is observed in the lower carbonate pelagic sedi-

ments based on void-ratio measurements from ODP leg 170 (Saffer et al., 2000). About 20 km farther downdip as temperatures increase to between approximately 60°–150° C along the plate boundary interface, clay mineral dehydration becomes a large factor in expulsion of fluids as clay minerals transition from smectite into illite (Bekins et al., 1994). These previous studies show that large amounts of fluids are expunged from subducted sediments throughout all stages of subduction. A major conduit for fluid flow is likely the decollement itself, as Tobin et al. (2001) observed offshore of the Nicoya peninsula, that the upper portion of the decollement is highly brecciated. Further, Teichert et al. (2005) found increasing percentages of Strontium isotopes progressively landward of the frontal prism, offshore Oregon in the Cascadia margin, indicating larger components of deeply-sourced fluids landward. Along with the decollement, Cloos (1984) observed that, in ancient subduction margins, highly brecciated melange formations dip landward and provide sufficient fracture permeability to support fluid flow.

Large sediment accumulations in accretionary margins help to absorb seismic reflection energy, lowering the vertical resolution of the decollement farther downdip. Costa Rica is an ideal setting for investigation of decollement properties because the relatively thin frontal prism does not degrade the seismic signal as much as actively accreting margins with thick sediment frontal prisms. Thus, the decollement reflection in our study area exhibits a high signal-to-noise ratio where higher frequencies are preserved, and higher vertical resolution of decollement-level seismic reflection events is on the order of 10 to 20 m depending on the distance from the trench axis. A "soft" seafloor with a seismic reflection coefficient of approximately 0.16 (von Huene et al., 1985), water depths approximately 2.6 km seaward of the trench axis, and only marginal ocean currents provide an excellent setting for surface 3D seismic reflection data acquisition. These conditions, in conjunction with a well-developed decollement near the frontal wedge, allow for high-

resolution 3D seismic data with high signal-to-noise ratio that is suitable for AVO analysis.

2.2 PREVIOUS WORK

Von Huene et al. (2004) introduced the concept of a frontal prism along the Costa Rica margin defined as a narrow band of accreted sediments landward of the trench that is highly deformed and provides a source of infill to subducting topographic lows. Approximately 10 km landward from the trench axis, von Huene et al. (2004) interpret a crystalline backstop that reduces data quality of reflections below. At the base of the frontal prism exist subducted sediments that have undergone dewatering and compaction from between 20% to 60%, showing sufficient permeability within the sediments to allow for initial dewatering (McIntosh and Sen, 2000).

Over long time scales, typical accretionary wedges at convergent plate boundaries are presumed to be in a state of equilibrium and exhibit a fixed taper angle (Davis et al., 1983). This critical taper angle is a static approach to subduction zone mechanics and requires the assumption that the overlying wedge is in a state of compression and is on the verge of failure everywhere (Davis et al., 1983). In Figure 2.3, the stress normal to the subduction interface is σ_z^*, and is directly related to the overburden weight of the wedge, the angle of the plate interface, minus the effect of pore fluid pressure. The basal shear stress along a plane, τ_b, is given by

$$\tau_b = \mu_b * \sigma_z^* \tag{2.1}$$

where σ_z^* is the effective normal stress, and μ_b is the coefficient of basal friction (Davis et al., 1983; Byerlee, 1978).

The critical taper angle of subduction margins is a fundamental property of wedge characteristics. Figure 2.3 shows that the angle of the plate boundary interface dip, β,

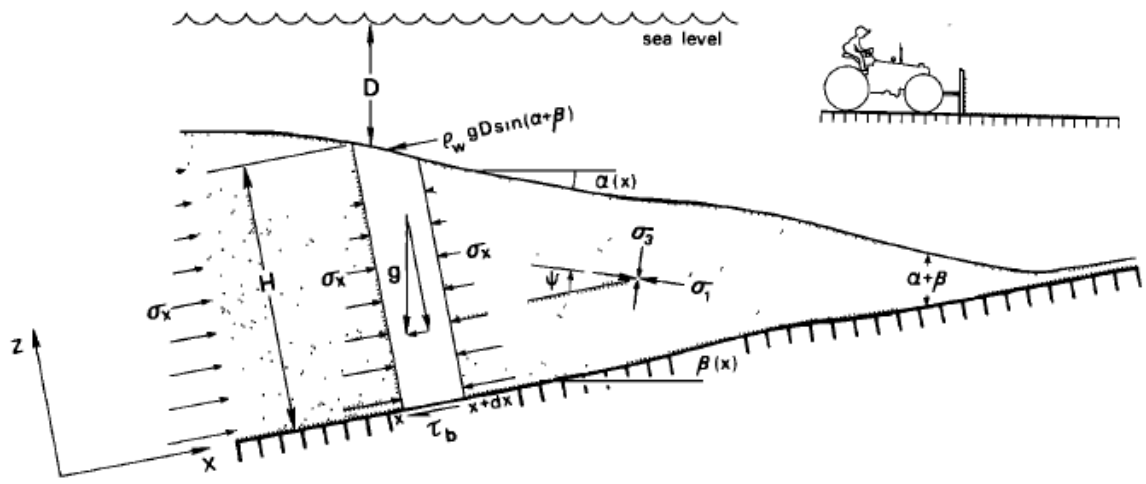

Figure 2.3: Davis et al. (1983) proposed the Coulomb wedge model that characterized the variables comprising subduction zone wedges. The wedge is assumed to be at critical failure everywhere and the plate boundary interface is modeled as a two-dimensional plane.

plus the angle of the seafloor surface with respect to horizontal, α, is the critical taper angle of a Coulomb wedge (Davis et al., 1983). The coefficient of basal friction, μ_b, is a necessary component that determines the taper angle of the wedge since higher taper angles generally correspond with higher basal friction coefficients. Therefore, knowledge of the taper angle may provide qualitative insight into the coefficient of basal friction along the plate boundary interface.

The Coulomb wedge model works reasonably well at explaining broad relationships between basal friction, using Byerlee's law, and taper angle of accretionary margins, yet problems arise when subduction margins are viewed on shorter time scales, or more detailed physical properties are needed. What we observe in contemporary margins is a snapshot in time of a prism that is likely in a state of dynamic disequilibrium, and observed taper angles are most likely not critical taper angles where the wedge is on the verge of failure. Wang and Hu (2006) addressed this problem and accounted for the impact of stress

variability during earthquake cycles and its effect on wedge morphology. Wang and Hu (2006) propose a dynamic Coulomb wedge where, during brief periods of seismic slip, the outer wedge is in a compressively critical state with increased pore pressure while the inner wedge remains in a stable state. After slip, the outer wedge then returns to equilibrium (Figure 2.4).

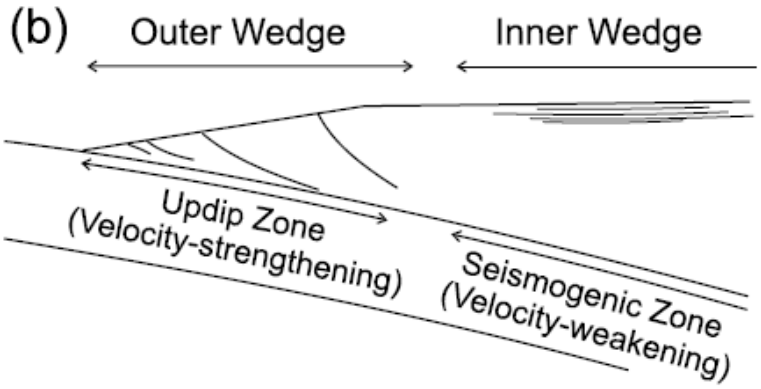

Figure 2.4: The outer wedge experiences seismic slip velocity strengthening behavior along the fault boundary and rebounds to equilibrium after seismic rupture compresses the outer wedge to critical taper (Wang and Hu, 2006).

The dynamic Coulomb wedge model asserts that the seismogenic zone beneath the inner wedge is characterized by velocity-weakening material. During large earthquakes, seismic rupture induces slip along a fault plane. As slip occurs at some velocity, the material becomes weaker, allowing for further propagation of slip both updip and downdip until all of the stored elastic strain is dissipated. The outer wedge of the model overlays velocity-strengthening material where slip along the plate boundary causes the interface to become stronger and able to dissipate seismic energy. These characteristics allow for strain accumulations to build up in the frontal prism as dissipated seismic energy in the outer wedge is stored as strain accumulation. Moreover, large amounts of strain accumulation will eventually favor elastic release of significant strain, creating the potential for tsunami

genesis.

Large seaward displacement of the outer wedge following seismic events was observed along the subduction margin offshore Japan during the 2011 M_w 9.0 Tohoku-Oki earthquake. Post-seismic slip estimates reveal approximately 30 m of displacement (Figure 2.5) near the trench that contributed to tsunami genesis (Ide et al., 2011). Similarly, comparison of GPS elevation data of the seafloor pre- and post-seismic slip show that after rupture, seafloor elevations are 0.8 m lower landward of the hypocenter and up to 3 m higher seaward of the hypocenter and are a result of immediate strain release (Sato et al., 2011). These data show the potential for large displacements of the frontal wedge following seismic events that leads to tsunami genesis. The significance of these findings is the ability of seismic rupture to propagate all the way to the trench axis and create very large displacements at the toe of the frontal prism.

The distribution of overpressure along the decollement along the Barbados Ridge shows a relatively thin ($\approx$ 30 m) zone where high pore pressure is presumed to be isolated within the decollement along what are interpreted as fluid migration pathways (Bangs et al., 1999). Offshore of the Nicoya peninsula, cores from ODP site 1070 within the frontal prism show strongly brecciated material in the first 24 m from the top of the plate interface followed by 14 m of non-brecciated ductile clay (Tobin et al., 2001). Chlorinity and C_3 (propane) measurements within the decollement zone indicate fluid isolation within the upper, brecciated section of the decollement. These studies provide evidence for non-trivial fluid movement into and out of the decollement via fracture pathways, setting up an environment for fluid content and overpressure heterogeneities to exist.

The Costa Rica margin has significant strike-oriented variability of basement and frontal prism structure. 3D seismic reflection data acquired offshore the Nicoya peninsula, Costa Rica, show large normal faults with approximately 300 m of offset that, in some

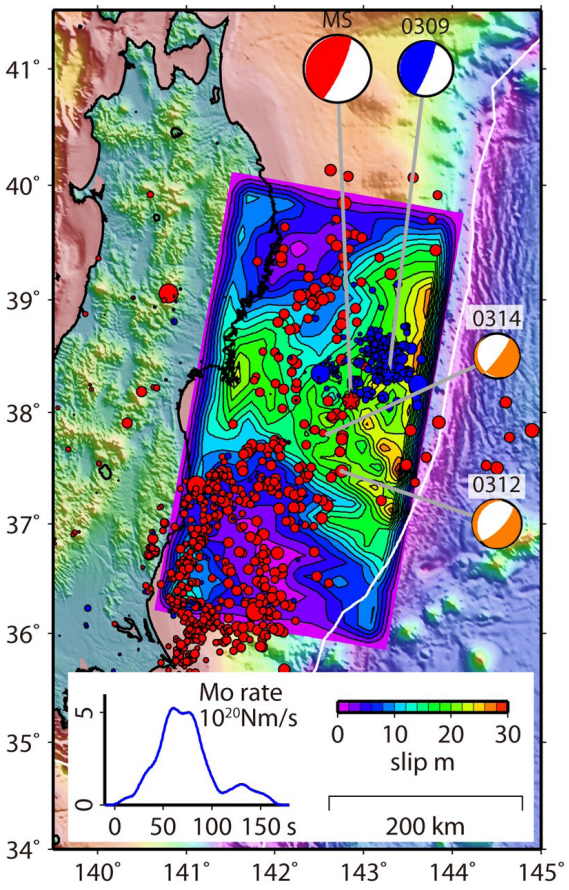

Figure 2.5: Ide et al. (2011) calculated displacements after the Tohoku-Oki earthquake offshore northeast Japan of up to 30 m at the trench axis, showing propagation of seismic energy along the plate boundary and terminating near the trench.

cases, are a key influence on the structure of the frontal prism (Shipley et al., 1992). Their study shows incoming hemipelagic sediments accreted to the upper plate via offscraping and structurally shortened from out-of-sequence thrust faulting. This area is also identified as a nearly reflection-free zone in the 3D seismic volume, which is likely a result of intense out-of-sequence faulting. Shipley et al. (1992) see evidence for prism taper highly affected by large-offset normal faults and unaffected in areas where the basement is smoothly subducting. Also identified is sediment underplating within the frontal prism as

the decollement responds to changes in wedge taper due to subducting basement normal faults. A negative reflection coefficient is observed along the decollement that Shipley et al. (1992) attribute to a velocity decrease across a highly deformed upper layer and a fluid-rich lower layer. No lower decollement reflecting interface is seen along the Costa Rica margin because there is no measurable abrupt change in velocity or density below the initial negative amplitude decollement reflection.

Plate boundary mechanics along the Costa Rica subduction margin and their relation to structure have been of particular interest as scientists try to better understand the processes involved with subduction erosion and identify the transition from aseismic to seismic behavior. Early investigations of subduction erosion propose that models with high basal friction, perhaps induced by subducting topographic features, remove material from the overriding plate where it is then carried downdip (Ranero and von Huene, 2000). Recent models proposed by von Huene et al. (2004), however, suggest that downthrown fault blocks are sufficiently filled with sediment and are not a major contributor to offscraping from the base of the overriding plate. Von Huene et al. (2004), Wang and Hu (2006), and Wang et al. (2010) instead propose a low basal friction approach where high pore pressures reach near-lithostatic values and fracture overriding material that is then removed and dragged down into the subduction channel. Wang et al. (2010) put forth a dynamic model of subduction erosion where erosion occurs during discrete periods of earthquake rupture when the plate boundary is weakest, and suggest low basal friction along the plate boundary during interseismic periods until earthquake rupture occurs. During rupture, velocity strengthening occurs along the aseismic zone of the plate boundary, inducing high basal friction and eroding portions of the overriding plate. Wang et al. (2010) then state that relaxation occurs during interseismic times, leading to normal faulting of the overlying wedge as seen in studies by Bourgois et al. (1984).

Chapter 3: Methods

3.1 SEISMIC DATA

3.1.1 Acquisition

3D multichannel seismic reflection data for this study were acquired in 2011 aboard the *R/V Marcus G. Langseth*. The total survey area was approximately 55 $\times$ 11 km and the acquisition configuration consisted of four hydrophone streamers, each 6 km long, with 468 channels per streamer. The receiver spacing in the cables was 12.5 m and the source interval was 25 m. Two laterally spaced 3300 in^3 airgun arrays were fired in an alternating sequence. The length of the streamer cables is critical because they provide sufficient source-receiver offset needed for AVO analysis at decollement-level reflection events. The size of the airgun array is sufficiently large to provide a seismic source wavelet strong enough to penetrate the subduction margin and record the plate boundary interface, yet sufficiently small enough to fire in short enough intervals to record high resolution and high fold reflection data.

3.1.2 Processing

Following acquisition, noisy traces were eliminated from the shot-sorted gathers and low frequency cable "strumming" was eliminated with a low-cut frequency filter from 0 to 6 Hz. Before bandpass filtering, predictive deconvolution was applied to the shot-oriented gathers to improve the effective source wavelet. A low frequency feature remained following the low-cut filter (Figure 3.1(1)), so the data were then band pass filtered between 0.1 Hz and 87 Hz using a Butterworth filter and successfully removed low and high frequency noise without artificially introducing high frequency noise into the gath-

ers. Figure 3.1 shows this effect on frequency spectra of a single shot gather after low-cut filtering but before bandpass filtering using the Butterworth filter (Figure 3.1(1)), after predictive deconvolution (Figure 3.1(2)), and after bandpass filtering (Figure 3.1(3)).

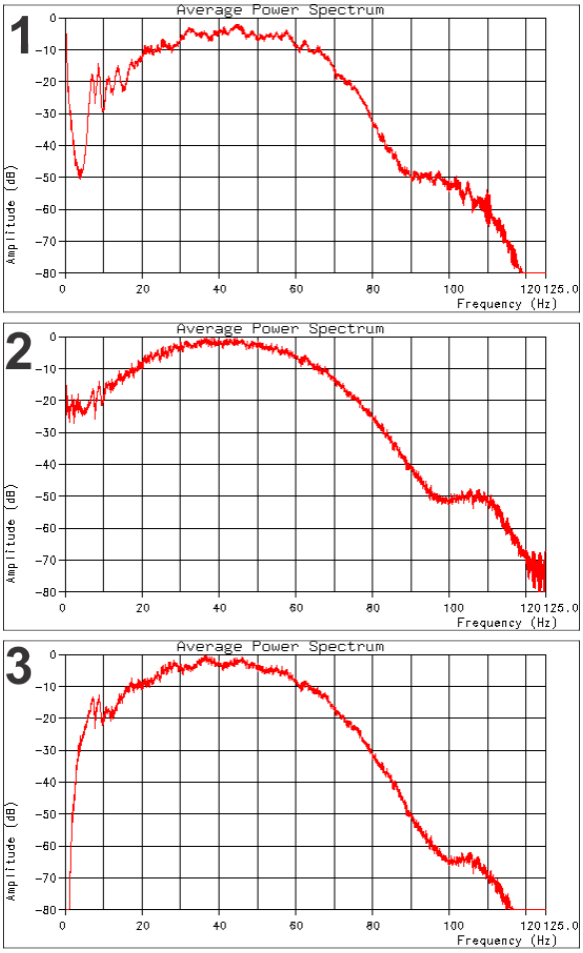

Figure 3.1: 1) Frequency spectrum for a CDP gather after low-cut filtering but before deconvolution and bandpass filtering where low frequency energy is still present, 2) after predictive deconvolution where there is excess energy above 100 Hz, and 3) after Butterworth bandpass filtering from 0.1 to 87 Hz.

For optimal AVO analysis, seismic data should be converted from minimum-phase to zero-phase wavelets. Doing so improves vertical resolution and focuses the energy of

the wavelet for optimal AVO analysis (Resnick, 1993). Tests performing spiking deconvolution on the dataset in order to produce zero-phase wavelets, however, decreased data quality and added unwanted artifacts. I instead performed predictive deconvolution, resulting in data that are minimum phase and does not induce artifacts. Predictive deconvolution is suitable for AVO analysis in this case because even though the data are not zero-phase, the AVO amplitude trends of the data are still preserved. Once filtering and deconvolution were performed, the data were sorted into common midpoint (CMP) gathers with a spatial CMP bin size of 37.5 $\times$ 25 m.

Vertical velocity analysis was performed on the entire survey area in order to create a velocity field suitable for normal move-out corrections and post-stack time migration. Finer detail velocity analysis was performed on a subset of the 3D volume that consisted of CMP gathers only within the tectonic frontal prism (10 $\times$ 15 km) where pre-stack Kirchhoff time migration was performed (Figure 3.2). Before application of normal moveout corrections with the velocity field, reflections within individual CMP gathers increase in arrival time with increasing offset in a hyperbolic manner. The goal of velocity analysis is to develop velocity functions used to correct these hyperbolic reflections to a constant zero-offset reflection time and also to be used to subsequently migrate diffracted wavefronts to their original reflection position. Reflections that are not perfectly horizontal after normal move-out (NMO) time correction have a "residual" velocity value that is the approximate difference between the velocity value from the earliest defined reflection event, the actual velocity value needed to properly correct the NMO effect, and variations in velocity values within the 3D volume.

Velocity values were manually picked from residual root-mean-square (RMS) velocity semblance plots every 10 reflection points in the strike direction (325 m) and every 20 reflection points along the dip direction (500 m) in order to produce a smooth

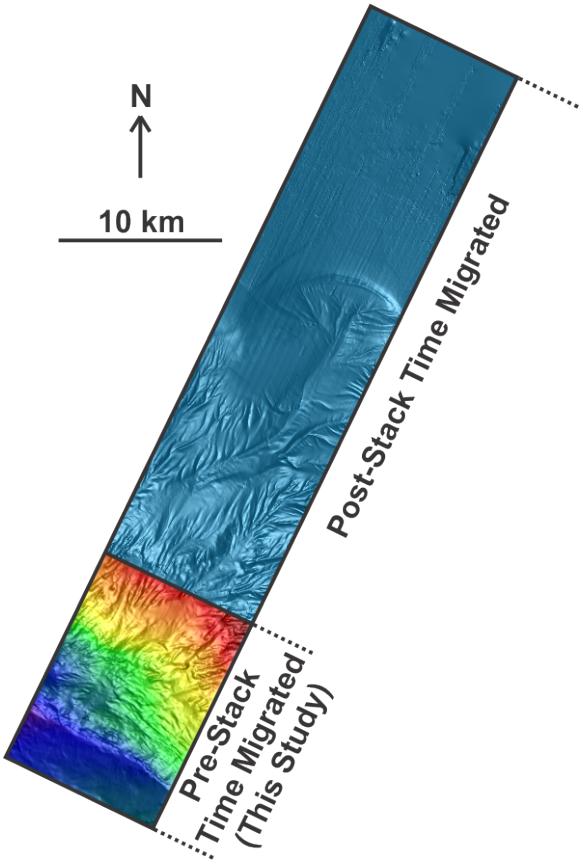

Figure 3.2: A seafloor map of the CRISP 3D seismic survey showing areas where the data were migrated post-stack (solid blue area) and where they were migrated pre-stack (multi-colored area). AVO analysis was performed on the pre-stack migrated data.

interval velocity volume that is consistent with the structure and geology of the accreted frontal prism. For migration, conversion from RMS velocity to interval velocity was accomplished using the Constrained Velocity Inversion technique developed by Koren and Ravve (2006) that is based on the Dix (1955) interval velocity equation. Five iterations of the velocity volume were performed so that the migrated CMP gathers were sufficiently corrected for AVO analysis.

Figure 3.3 shows the interval velocity volume used to migrate the CMP gathers.

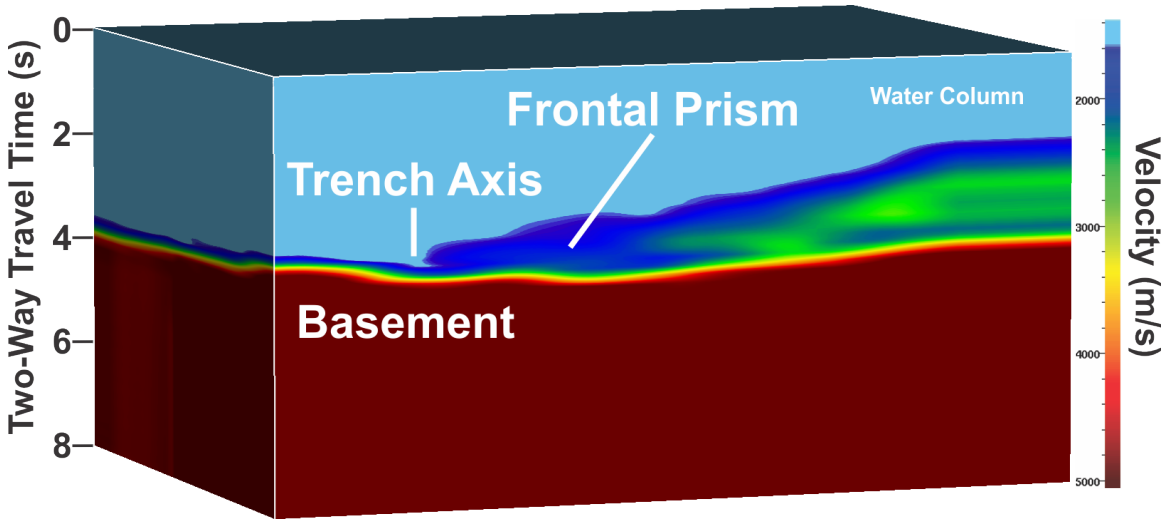

Figure 3.3: Interval velocity cube used for pre-stack Kirchhoff time migration. Sediment P-wave velocities in the frontal prism near the trench axis are below 2000 $m \cdot s^{-1}$ and become faster landward. Subducting oceanic basement velocities are between 4500 $m \cdot s^{-1}$ and 5000 $m \cdot s^{-1}$. A decrease in velocity of approximately 5% is observed between the top of the decollement and the top of the oceanic basement.

The seismic aperture within the frontal prism of the CRISP 3D survey is approximately 3000 m in the trench-perpendicular dip direction and approximately 750 m in the trench-parallel strike direction. Therefore, the P-wave velocity volume was extended at least 3000 m further landward than the downdip limit of the seismically observable decollement in order to properly migrate all possible decollement diffractions. Upper hemipelagic sediments seaward of trench are observed to have velocities between 1450 $m \cdot s^{-1}$ and 1600 $m \cdot s^{-1}$, consistent with shallow, uncompacted sediments. Pelagic carbonate sediments below the upper hemipelagics but above oceanic basement have velocities approximately 1600 $m \cdot s^{-1}$ to 2000 $m \cdot s^{-1}$. The seaward extent of the frontal prism has velocities between 1550 $m \cdot s^{-1}$ and 2000 $m \cdot s^{-1}$. Further landward, velocities in the frontal prism are above 2000 $m \cdot s^{-1}$ as sediments become more compacted and porosity decreases. Oceanic basement velocity is observed to be between 4500 $m \cdot s^{-1}$ and 5000 $m \cdot s^{-1}$ from these seismic

reflection data. The velocity is lower between the top of the decollement and the top of the subducting oceanic crust. Velocity inversions also exist landward within the frontal prism (Figure 3.3)

AVO analysis was performed using a commercially available software package, Paradigm^{TM} Probe®. Preconditioning of CMP gathers was kept to a minimum to preserve reflection amplitudes for the AVO response. Any modification to the gathers was applied equally across all offsets to preserve relative amplitude effects. The two corrections applied to the gathers were spherical divergence amplitude correction and use of a median filter of up to 3% to abate non-random noise generated from the Kirchhoff pre-stack time migration algorithm. Seismic amplitudes decay as waveforms propagate through the subsurface as a result of spherical divergence of the seismic wavefront (Yilmaz, 2001). Amplitude decay from wavefront divergence, A, is inversely related to the raypath radius, r, and was corrected for spherical divergence prior to AVO analysis using the following equation:

$$A(r) \propto \frac{1}{r}. \tag{3.1}$$

The AVO processing sequence used is outlined below:

1. *Low frequency cable noise attenuation (0 – 6 Hz)*
2. *Automated removal of noisy traces*
3. *Butterworth bandpass filter (0.1 – 87 Hz)*
4. *t^2 spherical divergence correction*
5. *Predictive deconvolution*
6. *Sort to CMP gathers*

7. *Iterative NMO velocity analysis*

8. *Kirchhoff pre-stack time migration*

Figure 3.4 is a fully processed CMP time migrated gather located within the frontal prism. Easily visible are the seafloor, bottom simulating reflector (BSR), decollement, and basement reflections. The decollement has a negative reflection coefficient caused by a velocity and density inversion. Very fast velocity ($\approx 4.5-5\ km\cdot s^{-1}$) basement beneath slow velocity ($\approx 2\ km\cdot s^{-1}$) cause basement reflections to destructively interfere with decollement reflections at offsets larger than approximately 3500 m. Therefore, offsets from 100 m to 3400 m were used for AVO analysis in order to avoid reflections with interference-altered amplitudes.

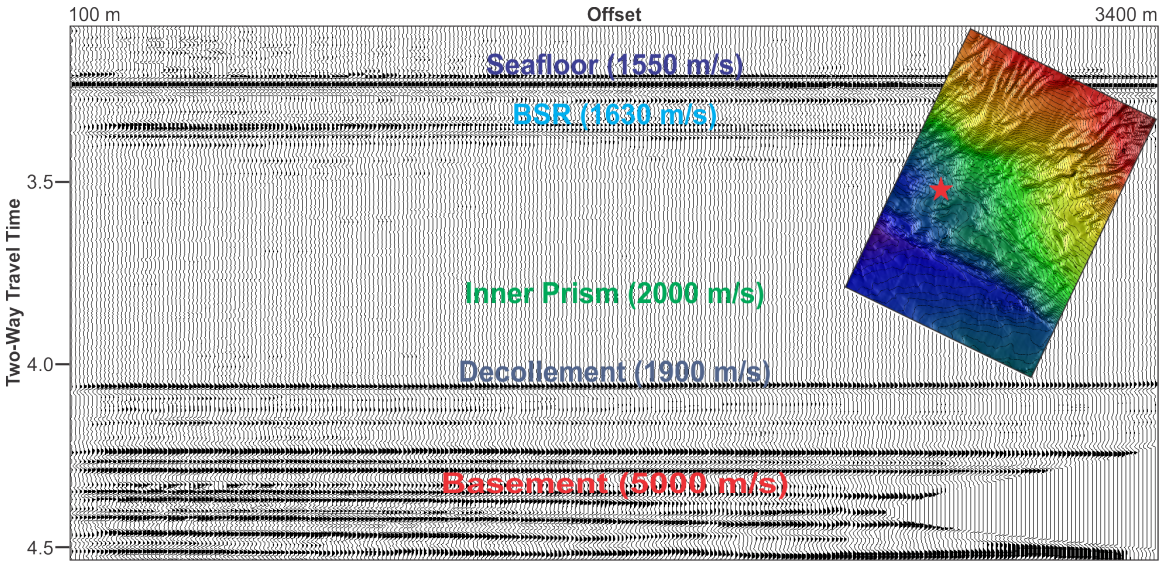

Figure 3.4: A fully processed CMP gather where the seafloor, BSR, decollement, and basement reflections are all clearly visible and the decollement is suitably flat for AVO analysis. The location of the gather is denoted by the red star on the seafloor inset map.

3.2 THEORY OF AMPLITUDE VERSUS OFFSET

Amplitude versus offset (AVO) response of seismic reflections from fluid-filled formations has been used in the oil industry as a tool to detect oil and gas saturation within hydrocarbon reservoirs based on reflection characteristics (Ostrander, 1984). Zoeppritz (1919) mathematically describes the reflection coefficient of a horizontal layered media as a function of the angle of incidence, $R_c(\theta)$, of an incoming seismic wavefront. Knowing details of seismic propagation allows us to describe angles of incidence in terms of source-receiver offsets. However, due to the complexity of the Zoeppritz equations, understanding physical rock properties from these equations proves to be difficult. As a result, a number of approximations to the Zoeppritz equations give geophysicists the tools to intuitively understand the relationship between $R_c(\theta)$ and selected inherent rock properties. Here we use the Shuey (1985) approximation to describe AVO response of the decollement because the equation relates the primary wave reflection coefficient, $R_{pp}(\theta)$, to variables that are relatively well constrained within our dataset. Shuey (1985) states that

$$R_{pp}(\theta) \approx A + Bsin^2(\theta) \tag{3.2}$$

where R_{pp} is the primary wave reflection coefficient at θ, the angle of incidence. A is the normal incidence reflection coefficient, and B is the AVO gradient. A is related to the contrast in acoustic impedance (ρV) across an interface, where ρ is the density of the formation and V is the formation velocity. With simplifying assumptions, B is related to the dynamic Poisson's ratio plus a component of the normal incidence reflection coefficient, A. This equation is valid for small contrasts in velocity and density, and angles of incidence up to about 30°, all of which are valid in this study. Note that B is a gradient of seismic reflection amplitude with respect to the square of the sine of the angle of incidence.

Since the change in amplitude with offset, B, is strongly influenced by Poisson's

ratio, σ, of the reflective media, it thus gives insight into the physical rock properties of the subsurface interface (Ostrander, 1984). When a static stress is applied to one end of a material, shortening in the direction of application is related to extension in the direction orthogonal to the force applied. The ratio of the change in lengths is referred to as Poisson's ratio. Poisson's ratio can be determined from observed pressure and shear wave velocities by:

$$\sigma = \frac{\frac{1}{2}\left(\frac{V_p}{V_s}\right)^2 - 1}{\left(\frac{V_p}{V_s}\right)^2 - 1}. \tag{3.3}$$

The dynamic Poisson's ratio is related to the gradient, B, as follows

$$B = EA + \frac{\Delta\sigma}{1-\bar{\sigma}^2} \tag{3.4}$$

where

$$E = F - 2(1+F)\frac{1-2\bar{\sigma}}{1-\bar{\sigma}} \tag{3.5}$$

and

$$F = \frac{\frac{\Delta V_p}{\bar{V_p}}}{\frac{\Delta V_p}{\bar{V_p}} + \frac{\Delta\rho}{\Delta\bar{\rho}}} \tag{3.6}$$

and $\bar{V_p}$ is the average pressure wave propagation velocity, and $\bar{\sigma}$ is the average Poisson's ratio between the two interfaces (Castagna, 1993; Mavko et al., 2009). It should be noted that variables E and F themselves do not represent meaningful geophysical properties and are instead used as place holders to understand the meaning of the AVO gradient, B.

As shown above, the AVO gradient, B, is heavily influenced by the contrast in the dynamic Poisson's ratio, which itself may be defined by $\frac{V_p}{V_s}$, a ratio that we can extract from the seismic data, along with previous laboratory experiments. Normal incidence

reflectivity, A, is simply the reflection coefficient of the interface at normal angle of incidence and is given by the contrast in acoustic impedance between the upper and lower layer.

From these conditions, and with careful velocity estimation, it is possible to predict the AVO response by systematically defining V_p and V_s as we would expect in an overpressure environment such as the decollement shear zone beneath the frontal prism. As V_p and V_s change, so do both A and B. Model simulations of A and B values for a contrast between normally pressured and overpressured zones define limits of A and B that may be used to interpret actual A and B values from real data. It must be noted that other subsurface conditions may, in principle, yield similar A and B values, yet contrasts in both acoustic impedance and independent contrasts in the dynamic Poisson's ratio, give us confidence in our interpretations.

3.3 Modeling of AVO Response to Fluid Pressure

Before actual analysis of AVO information was performed on the seismic reflection data, a full suite of models were calculated in an effort to ascertain the driving mechanism of AVO response in an undercompacted, highly-overpressured, brine-filled environment. The four main questions that need to be addressed before simulating the AVO response along the decollement interface are:

1. *How thick is the decollement?*
2. *How does pressure change when transitioning from the overlying frontal prism to the underlying shear zone?*
3. *What are the bulk densities across such a transition?*

4. *How do V_p and V_s vary as fluid content increases within the overpressured shear zone?*

3.3.1 Pore Pressure

The Ocean Drilling Program (ODP) leg 170 drilled into the frontal prism offshore the Nicoya peninsula in 1996 in effort to quantify changes in bulk density, seismic velocity, and pressure across the decollement interface. Boreholes at sites 1043 and 1040, in Figure 3.5, crossed the decollement zone where it was found to be 9 m and 38 m thick, respectively (Tobin et al., 2001).

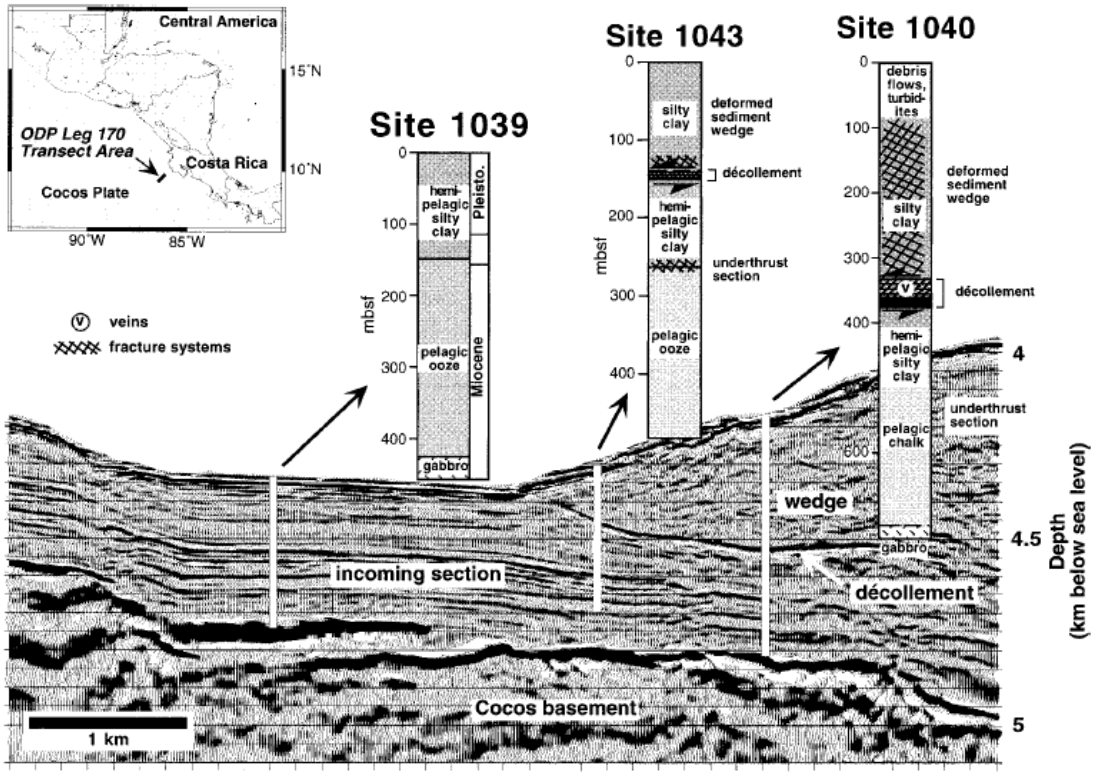

Figure 3.5: Seismic profile in depth from McIntosh and Sen (2000) offshore the Nicoya peninsula shows locations of well sites 1043 and 1040 from ODP leg 170. A simplified stratigraphic section accompanies each well location (Tobin et al., 2001).

Moderately increased pore pressures of approximately 25% lithostatic pressure ($\lambda^* = 0.25$) are presently found in the frontal prism above the decollement offshore of the Nicoya peninsula at a depth of approximately 125 m (Davis and Villinger, 2006). However, for modeling purposes, pore pressures ranging from hydrostatic to lithostatic values are constrained only within the decollement in order to isolate the response from the decollement. Overpressures are represented here by the Hubbert-Rubey (1959) fluid pressure ratio, λ^* (Equation 3.7), defined as the ratio of pore pressure, P_{pore} to lithostatic overburden pressure, P_{lith}, normalized to the hydrostatic pressure, P_{hyd} (Hubbert and Rubey, 1959; Bilotti and Shaw, 2005; Saffer and Tobin, 2011). When $\lambda^* = 0$, the pore fluid is at hydrostatic pressure, and when $\lambda^* = 1$, the pore fluid is at lithostatic pressure.

$$\lambda^* = \frac{P_{pore} - P_{hyd}}{P_{lith} - P_{hyd}} \tag{3.7}$$

A median decollement depth was estimated for construction of the pressure model. At this location, the depth of the water column, D_w, is 2.7 km, the depth from the seafloor to the decollement, D_l, is 800 m, and the thickness of the underthrust sediments is 100 m.

The hydrostatic pressure at the top of the decollement, P_{hyd}, is a function of D_w, D_l, the density of water, ρ_w, and the acceleration of gravity, g.

$$P_{hyd} = (D_w + D_l)\,\rho_w g \tag{3.8}$$

Lithostatic pressure at the depth of the decollement is a function of D_w, D_l, ρ_w, density of the overlying rock, ρ_l, and g. The density of seawater used is: $\rho_w = 1050\,kg \cdot m^3$, and the density of the frontal prism is extracted from ODP site 1070 bulk density estimates where $\rho_l = 1930\,kg \cdot m^3$. The equation for lithostatic pressure is as follows:

$$P_{lith} = D_w \rho_w g + D_l \rho_l g \tag{3.9}$$

Varying the pore pressure is achieved by changing λ^* between hydrostatic and lithostatic pore fluid pressures. Equations used in the model are shown below in Equations 3.10 and 3.11 where the pore fluid pressure, P_{pore}, is defined as:

$$\frac{dP_{pore}}{dm} = \lambda^* \left(\frac{dP_l}{dm} - \frac{dP_w}{dm} \right) + \frac{dP_w}{dm} = \lambda^* \left(\rho_l g - \rho_w g \right) + \rho_w g \tag{3.10}$$

$$P_{pore} = \left(D_w + D_l \right) \frac{dP_{pore}}{dm} - \left(\frac{dP_{pore}}{dm} - \frac{dP_w}{dm} \right) D_w \tag{3.11}$$

Figure 3.6 is a graphical representation of the pressure regime at near lithostatic values when $\lambda^* = 0.95$. The blue line is hydrostatic pressure, the green line is lithostatic pressure, and the red line is the pore fluid pressure. Pore fluid pressure is calculated using Equation 3.11 by incrementally varying the pore fluid pressure gradient, dP_{pore}, from hydrostatic to lithostatic pressure.

3.3.2 Bulk Density

These borehole data show a sharp decrease in bulk density across the decollement from approximately $1.9\, g \cdot cm^3$ to $1.7\, g \cdot cm^3$ that continues until drilling ceased near the top of the subducting oceanic crust (Figure 3.7). An abrupt decrease in bulk density across the decollement interface indicates that hemipelagic sediments are undercompacted. Saffer et al. (2000) show that subducted sediments off the Nicoya peninsula at ODP site 1040 and 380 m depth, have a fluid content of approximately 46% of what was initially subducted at the trench, and experience increased pore fluid pressures in excess of 1.3 MPa to 3.1 MPa (Saffer et al., 2000). Bangs et al. (1999) found similar results within the Barbados Ridge

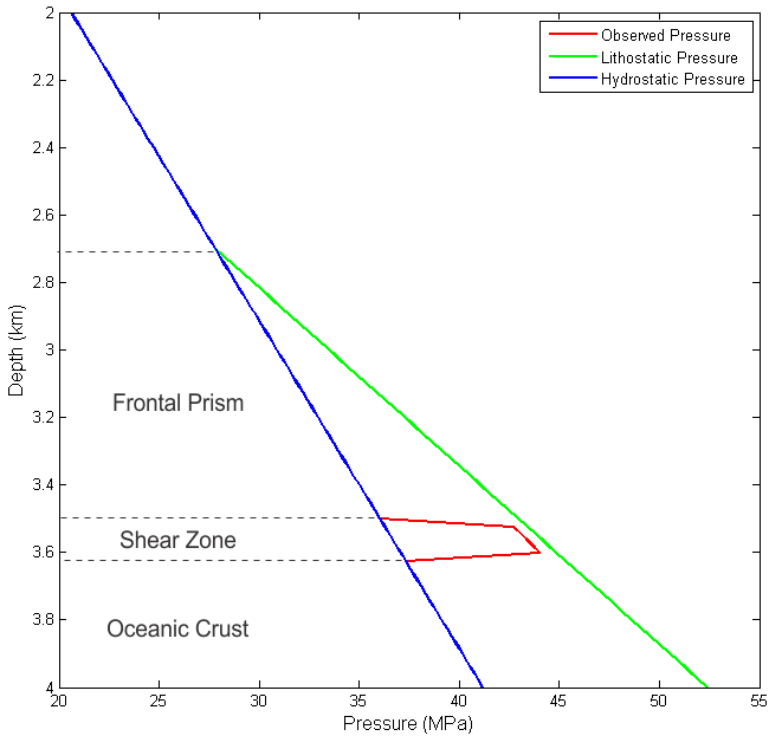

Figure 3.6: The decollement is modeled an isolated zone of overpressure; shown here is $\lambda^* = 0.95$.

accretionary wedge, showing bulk density measurements lower within the decollement as compared to the overlying wedge, and interpreted these areas as undercompacted and potential areas of increased porosity and permeability.

Bulk densities from site 1040 within the overlying frontal prism are between 1.9 $g \cdot cm^3$ and 1.95 $g \cdot cm^3$, whereas the bulk density within the first 10 m of the decollement is approximately 1.7 $g \cdot cm^3$. Overpressure may be characterized by undercompaction and excess porosity. A key assumption in this environment is the correlation between fluid content and fluid pressure. McIntosh and Sen (2000) show areas where incoming sediments off the Nicoya peninsula undergo compaction between 20% and 60%, and active dewatering is occurring via fractures within the subducting sediments or perhaps along

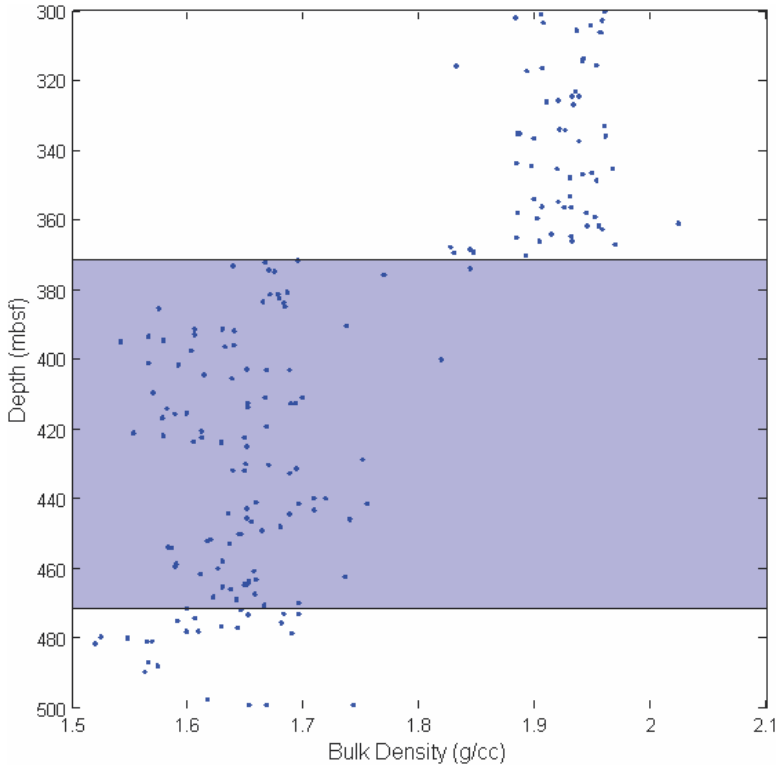

Figure 3.7: Bulk density data from ODP site 1040. Densities used in the model are $\rho = 1.9\,g \cdot cm^3$ for the upper layer and $\rho = 1.7\,g \cdot cm^3$ for the decollement zone.

basement normal faults. With active dewatering occuring, any increase in pore fluid content of subducted hemipelagic sediments is likely a result of inhibited compaction that results in anomalously high pore fluid content and pore fluid pressures. With this assumption in mind, a three-layer, discrete pressure model is proposed. Layer 1 is 100 m of overlying frontal prism; layer 2 is 100 m thick that represents the decollement fault zone where pore fluid pressure increases; and layer 3 is 100 m of subducting oceanic basement. I represent the decollement here as a single impedance contrast at the base of the overlying prism that isolates the overpressure zone. Bulk density values remain consistently low and velocities are fairly constant until the oceanic basement is reached; therefore, no bottom decollement reflection is modeled, nor is it seen in the 3D seismic reflection profiles.

3.3.3 Seismic Propagation Velocity Estimation

Estimation of seismic P- and S-wave velocities is critical to calibration of AVO analysis because increases in fluid content often have a pronounced effect on seismic pressure wave (V_p) and shear wave velocities (V_s). Figure 3.8 shows laboratory seismic velocity observations on samples consisting of a medium- to fine-grained sand that show a decrease in velocity as a power-law function of decreasing differential pressure (Prasad, 2002).

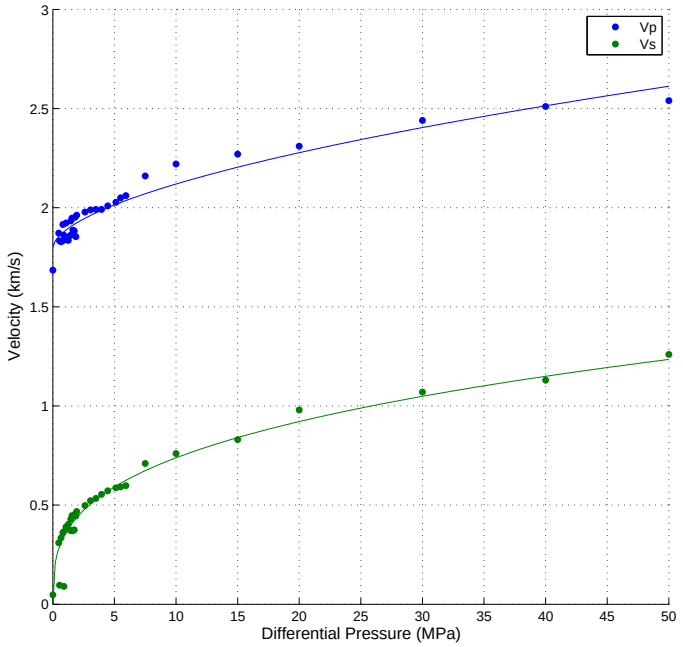

Figure 3.8: Laboratory observations of V_p and V_s on medium- to fine-grained, fluid-saturated sand (Prasad, 2002). As P_d approaches close to zero, the gradient of V_s increases faster than that of V_p.

The best fit power-law functions are as follows:

$$V_p = 0.083958 * P_d^{0.58017} + 1.8 \; km \cdot s^{-1} \tag{3.12}$$

$$V_s = 0.35379 * P_d^{0.31947} \; km \cdot s^{-1} \tag{3.13}$$

where P_d is the differential pressure defined as

$$P_d = P_{lith} - P_{pore} \tag{3.14}$$

where P_{lith} is the lithostatic overburden pressure and P_{pore} is the pore fluid pressure.

As pore pressure increases (differential pressure decreases), the model data show V_p and V_s decreasing at slightly different rates. High fluid pressure (low differential pressure) has a more pronounced effect on V_s than it does on V_p due to decreases in grain-to-grain contact. Pore fluids at high pore fluid pressure can decrease grain-to-grain contact as the internal fluid pressure approaches overcoming the overburden stress. Once this occurs, the shear strength, i.e., rigidity, of the sediments is drastically reduced and may even approach zero, yet the compressional strength of the fluid-filled sediments will never approach zero but will instead approach the compressional strength of the fluid.

Figure 3.9 is a block model of the input parameters used to calculate the anticipated AVO attributes. Figure 3.9 shows the input parameters in both a background hydrostatic state and at near lithostatic pressures where $\lambda^* = 0.95$.

3.3.4 Shuey Approximation

The Shuey approximation to the Zoeppritz equations is a useful simplifying tool when performing AVO analysis because the parameters used in the Shuey equations have quite meaningful geophysical significance (Castagna, 1993). The parameters discussed above are from model inputs, and the results serve as a baseline AVO response of what to expect before actual analysis of extracted AVO attributes from the 3D seismic volume. Reflection coefficients over angles of incidence spanning 0° to 40° are calculated for all overpressures ranging from $\lambda^* = 0 - 1$ in increments of 0.05. The maximum angle of incidence was estimated from the survey parameters and is within the small-angle assumption

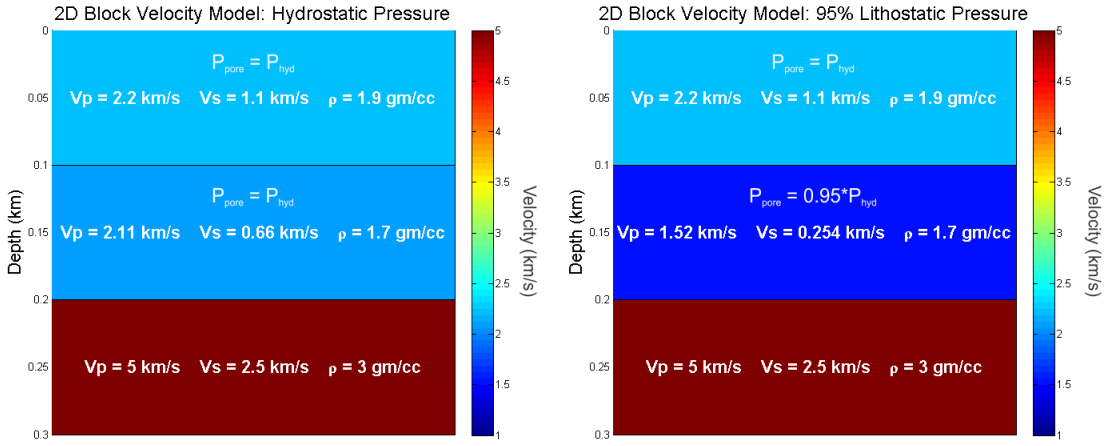

Figure 3.9: Block models of hydrostatic pressure (left) and $\lambda^* = 0.95$ (right) within the decollement. Density is held constant, and V_s and V_p decrease as power-law functions with increasing pore fluid pressure.

associated with the Shuey approximations in order to limit incidence angles to reasonable values.

Figure 3.10 shows the calculated AVO response from the model that includes the reflection coefficient, $R(\theta)$, as a function of angle of incidence, θ, for a wide range of overpressures. Colored plots are used to show reflection coefficient curves for various scenarios of increased pore pressure. For these results, I suggest pressure increases within the underthrust sediments, fluid content within the underthust sediments increases, which results in a negative velocity gradient that creates a large, negative impedance contrast. Moreover, as pore pressure increases, the gradient of the reflection coefficient curves becomes increasingly more positive, meaning that reflections at large angles of incidence become weaker and less negative.

AVO analysis is generally performed to evaluate possible hydrocarbon saturation. Gas concentrations have a more pronounced effect on V_p of the host rock (Figure 3.11)

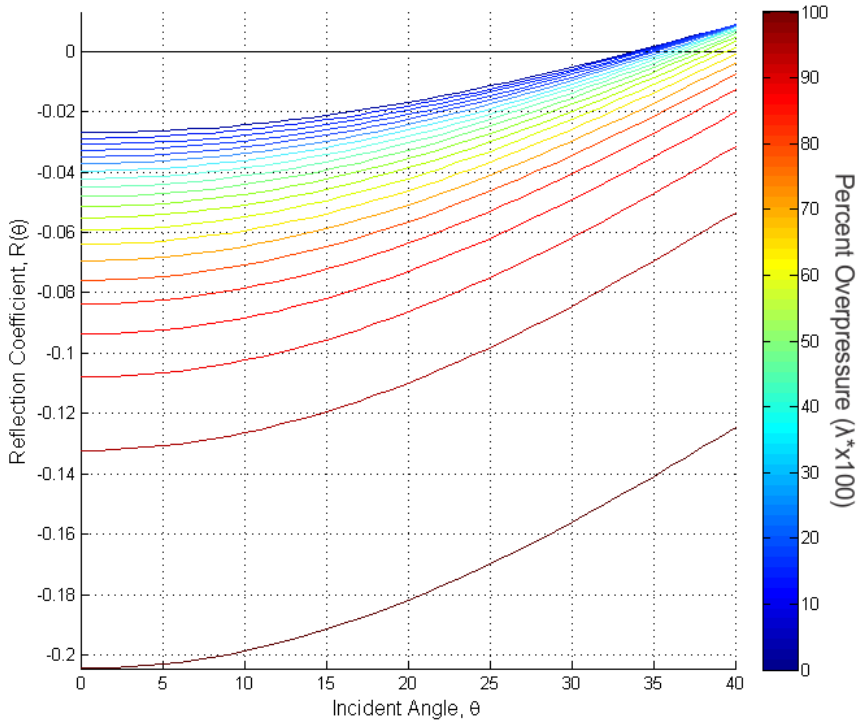

Figure 3.10: As pore pressure increases, the zero offset reflection coefficient, $R(0)$, becomes progressively more negative. Over all pressure regimes, the reflection coefficient becomes less negative as the incident angle increases. Note that the P-wave velocity and density of the lower (overpressured) layer is less than the overlying layer.

when gas concentrations are above approximately $5-10\%$ (Ostrander, 1984). A decrease in V_p is fundamentally caused by a decrease in the incompressibility of the bulk rock resulting from the increasing compressibility of gas-saturated pore fluid. This causes a noticeable drop in Poisson's ratio (Figure 3.11). Since the shear velocity is only slightly changed due to the gas saturation, this then leads to a sharp decrease in the $\frac{V_p}{V_s}$ ratio, or the dynamic Poisson's ratio. In fact, as gas concentration increases in a reservoir, the shear velocity actually increases because the rigidity of the formation is unchanged, but the density of the fluid is less as liquid fluids are replaced with gaseous fluids (Figure

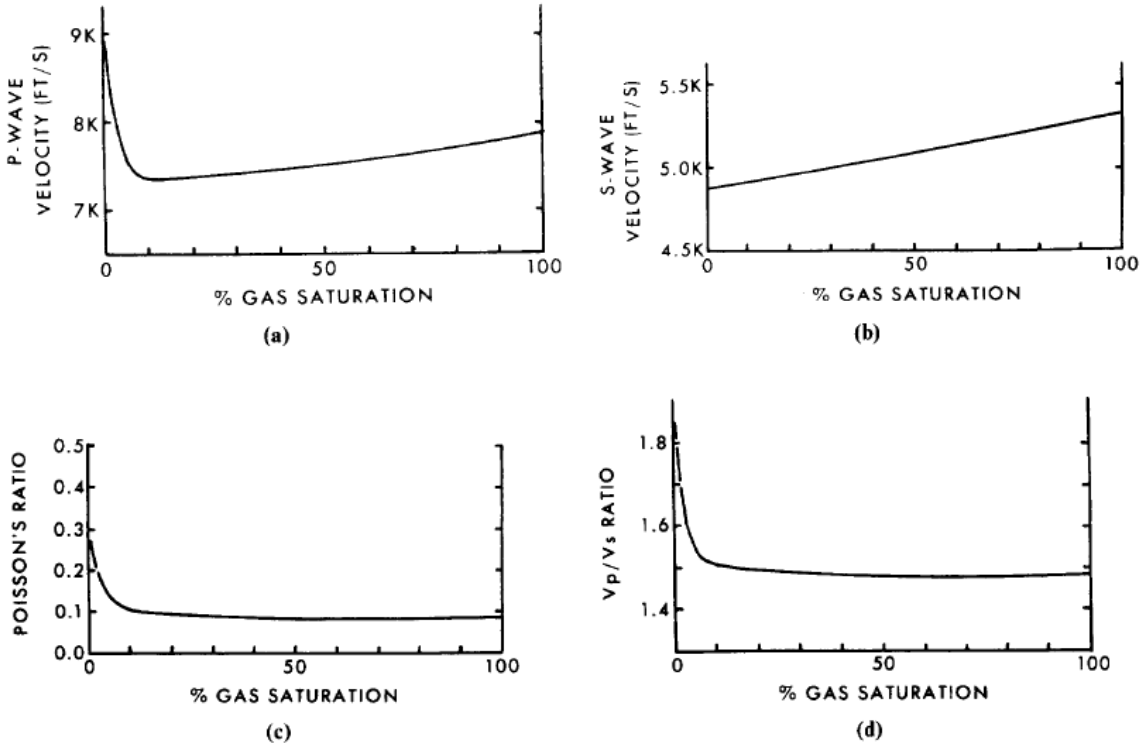

Figure 3.11: Small percentages of gas saturation decrease the velocity of the rock enough to have a significant effect on Poisson's ratio (Ostrander, 1994). Focusing on brine-filled sediments in this study induces subtle increases in Poisson's ratio as fluid content increases.

3.11). This decrease in density, with no change in rigidity, leads to an increase in S-wave velocity. Gas content causes the amplitude gradient, B, to become anomalously negative as a result of lower values of Poisson's ratio and will decrease, often quite significantly, the value of the negative reflection coefficient (Castagna et al., 1998) (Figure 3.12).

Figure 3.12 shows the AVO classification schemes introduced by Rutherford and Williams (1989), with the addition of a class IV anomaly by Castagna et al. (1998), and classify rock formations in terms of shales overlying gas-bearing sands. Class I anomalies are shales that overlay a high-impedance sand where the reflection coefficient decreases with offset. Class II anomalies have low normal-incidence impedance where the reflection

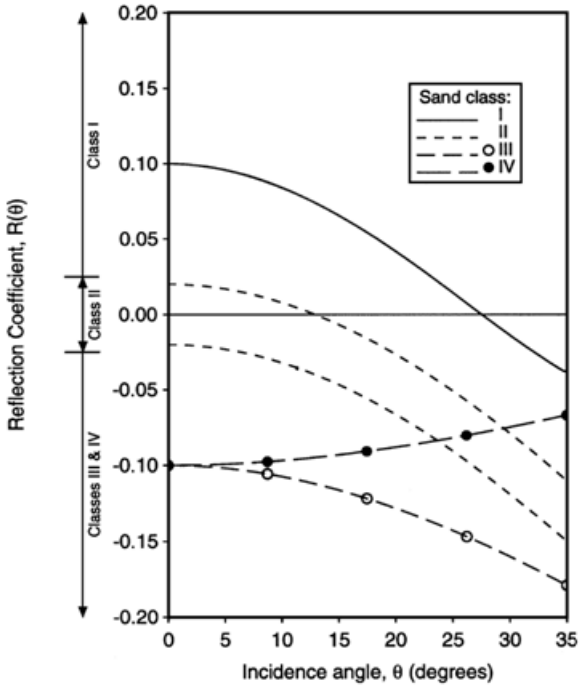

Figure 3.12: Castagna et al. (1998) AVO classification scheme. Overpressured, brine-filled hemipelagic sediments are similar to class IV AVO anomalies, where the reflection coefficient ($R(\theta)$) becomes less negative as the incidence angle increases.

coefficient decreases with increasing offset, and class III anomalies are negative reflections that become more negative with increasing offset (Castagna et al., 1998). Class III AVO anomalies are often observed in what are known as "bright spots" in the Gulf of Mexico and are gaseous reservoirs underlying a sealing formation. Castagna et al. (1998) introduce a class IV AVO anomaly where a porous gas-saturated sandstone is above a hard shale and has a negative reflection coefficient that becomes smaller with increasing incidence angle. Modeling of a brine-saturated decollement closely mimics this class IV AVO anomaly, even though the fundamental lithologies and environments are vastly different.

Increases in total fluid content within the decollement should cause a similar, but opposite, effect on the pressure wave velocity. As pore pressure increases to lithostatic

values, fractures inherent within the shear zone may open and expand, leading to an increase in the porosity and fluid content. The ratio of incompressible fluid to relatively compressible hemipelagic host rock will effectively increase Poisson's ratio, causing the AVO gradient to become more positive.

Analyzing reflection amplitude variation directly from reflection coefficient curves may be ambiguous, so a tool known as the AVO crossplot is used to simultaneously assess changes in reflection amplitude variation and amplitude gradient. In AVO analysis of hydrocarbon reservoirs, B and A values are extracted in areas known to be non-hydrocarbon bearing and crossplotted as B vs. A. Recall that the AVO parameter, A, is an expression of the normal incidence amplitude response ($\Delta\rho V_p$), and AVO gradient, B, is related to the dynamic Poisson's ratio. The resulting crossplot delineates a background trend of normal AVO response (Castagna et al., 1998). Plotted points away from the background trend are interpreted as anomalous characteristics such as the presence of gas and oil, increased pore pressure, or perhaps other effects. The most pronounced effects occur at the reflectivity interface between a gas saturated reservoir below a brine-saturated formation or at the gas/liquid fluid boundary.

Rutherford and Williams (1989) introduced the quadrant numbering system (Figure 3.13) based on the reflection coefficient curve in Figure 3.12. Many larger-porosity, gas-saturated hydrocarbon reservoirs overlain by a brine-saturated sealing formation will often create a negative normal-incidence reflection coefficient that has a negative amplitude gradient, becoming more negative as incidence angle increases. This response will plot in quadrant III of the quadrant system and is referred to as a class III AVO anomaly in Rutherford and Williams (1989). Overpressured hemipelagics will plot in quadrant II and are very similar to the class IV AVO anomaly shown in Figure 3.12.

It is helpful for seismic attributes to be strongly correlated to an understandable

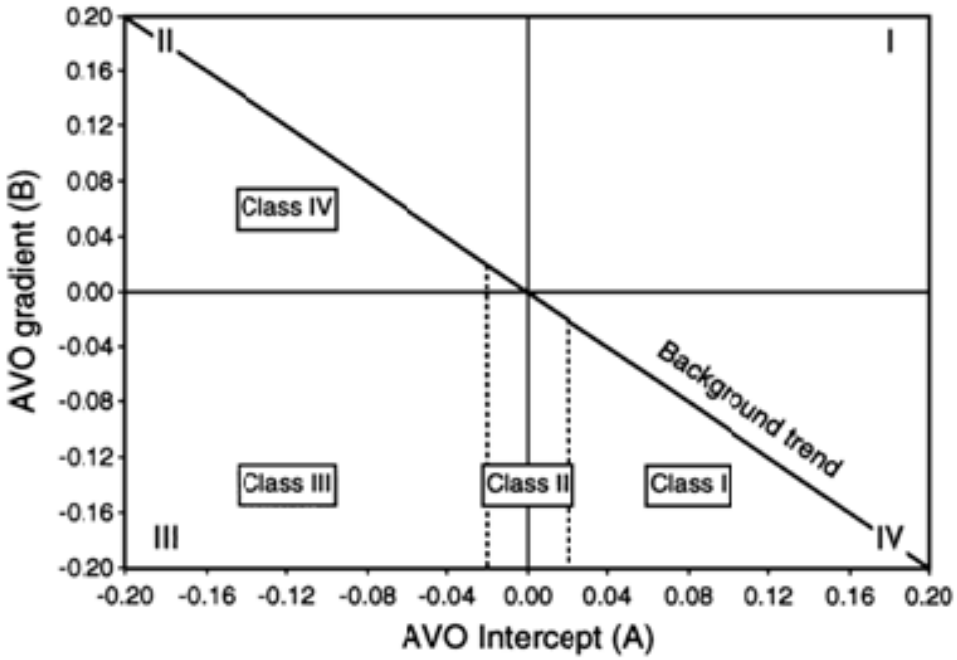

Figure 3.13: AVO crossplot classification system from Castagna et al. (1998). AVO anomalies along the decollement tend to plot in quadrant II.

geophysical quantity, and accurate knowledge of Poisson's ratio is valuable to pore pressure estimation. Equation 3.4 defines B as a function of Poisson's ratio plus a term proportional to the normal incidence reflection coefficient. Subtracting A from B yields a value that is primarily a function of Poisson's ratio, σ (Equation 3.3), and has a nearly linear trend (Figure 3.14). Values of Poisson's ratio in this environment are extremely high because the fluid content in the subducting sediments is very high, causing values of Poisson's ratio to be near that of extremely incompressible pure water. Further, an increase in pore pressure leads to an increase in B-A (Figure 3.15). Here, the assumption is that high pore fluid contents reside in areas that are undercompacted, and it is theorized that an effect of undercompaction is elevated pore fluid pressures. Therefore, an increase in fluid content causes Poisson's ratio to increase as a result because the material is becoming

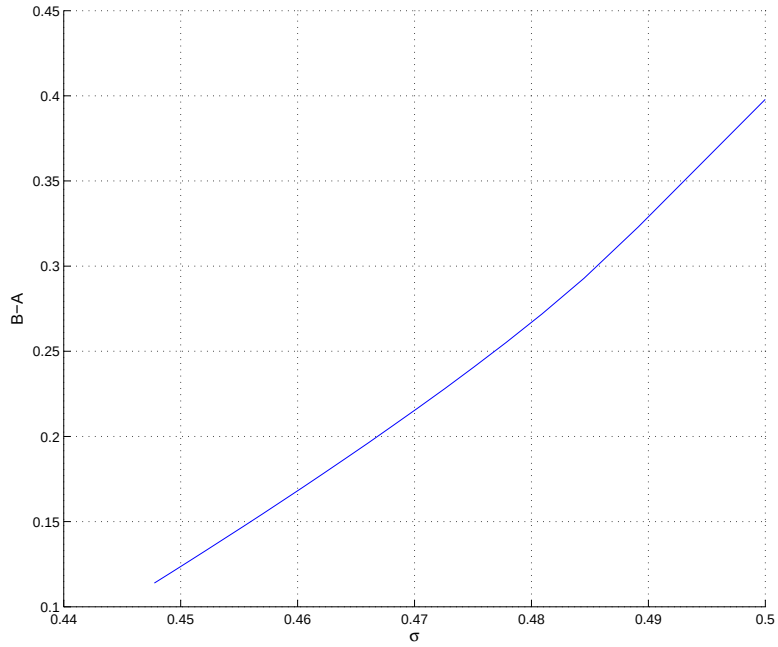

Figure 3.14: Crossplot of Poisson's ratio and B-A for my modeled data shows a nearly linear correlation between the two. Higher values of Poisson's ratio correspond to higher B-A values. Values of Poisson's ratio are extremely high and near that of a pure fluid due to high pore fluid content in subduction zone sediments. Values of B-A and Poisson's ratio are from decollement model AVO calculations.

more incompressible.

Since the effect of the dynamic Poisson's ratio on E in equation 3.5 is relatively minimal, subtracting EA from B in equation 3.4 gives us

$$B - EA = \frac{\Delta\sigma}{1-\bar{\sigma}^2} \tag{3.15}$$

and is strongly related to the dynamic Poisson's ratio. Since E cannot be directly calculated from seismic data, subtracting the observable attribute A from B more accurately estimates the dynamic Poisson's ratio than B alone.

$$B - A \propto \frac{\Delta\sigma}{1-\bar{\sigma}^2} \tag{3.16}$$

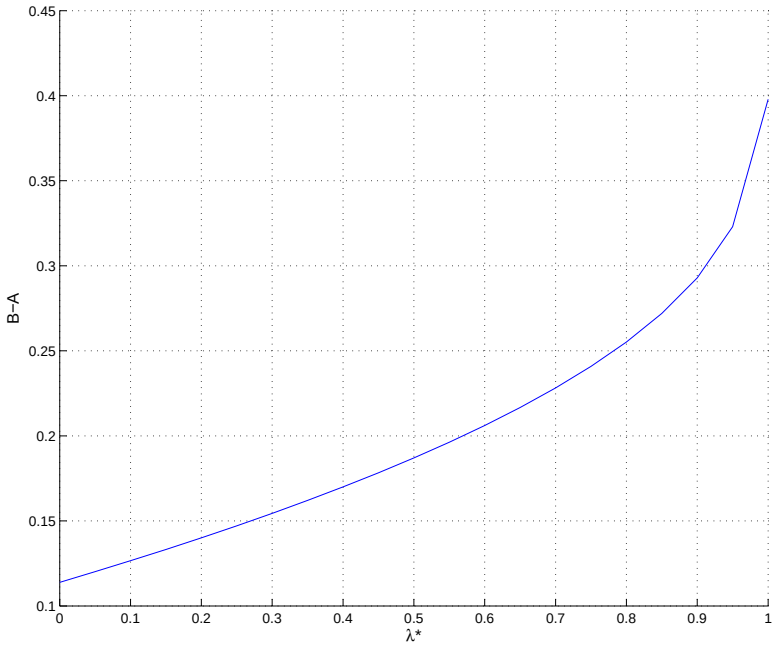

Figure 3.15: A strong, positive, but non-linear correlation between pore fluid pressure (λ^*) and B-A. As fluid content increases, pore fluid pressures are presumed to rise as well, resulting in a material that is more incompressible at high pore fluid pressures.

Modeling the ratio $\frac{B}{A}$ shows that it is similar to a class IV AVO anomaly where the decollement reflection coefficient becomes less negative with increasing offset. At background hydrostatic pore pressure, $\frac{B}{A} \approx -3.21$, and $\frac{B}{A} \approx -0.95$ at lithostatic pressures where Poisson's ratio increases to nearly that of water, $\sigma = 0.5$ (Figure 3.16). The difference in Poisson's ratio between lithostatic and hydrostatic pressures, $\sigma_{lithostatic} - \sigma_{hydrostatic}$, is only 0.0522 but appears to be enough of a difference to produce noticeable AVO anomalies. However, anomalous AVO behavior may only be noticeable at near-lithostatic values when σ is substantially high enough to overcome data noise and cause detectable changes in B.

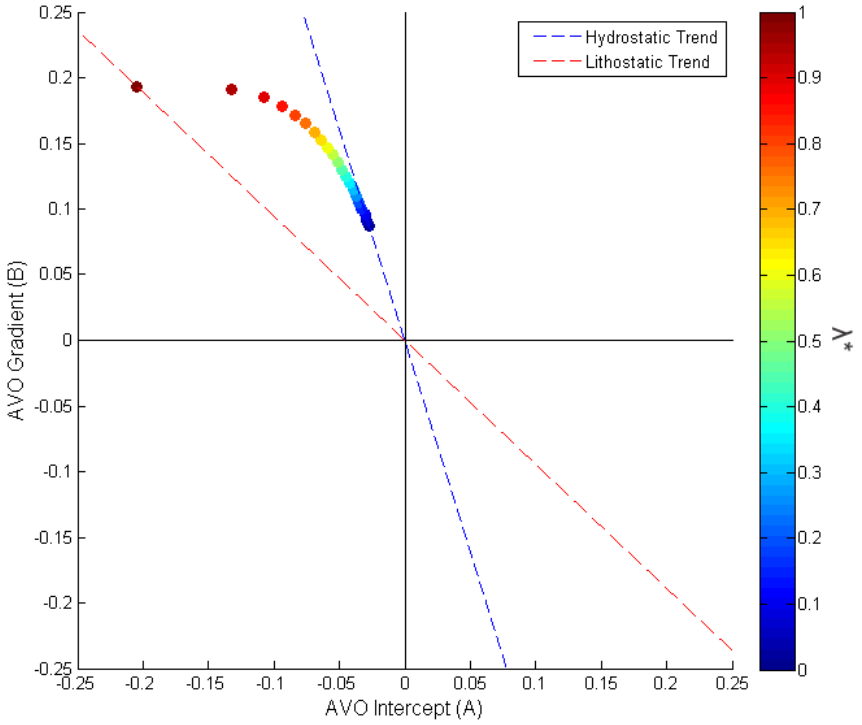

Figure 3.16: Crossplot of modeled AVO response at pressures from $\lambda^* = 0 - 1$. AVO slopes become less negative as pore pressures increase.

3.4 Seismic Attributes

3.4.1 AVO Attributes

Normal incidence reflectivity, A, and amplitude gradient, B, were calculated within the entire 3D volume of the frontal prism over all reflection times and traces. Two principal horizons were interpreted for AVO analysis: the decollement reflection and a reflector seaward of the trench within the hemipelagic sediments. AVO attributes, A, and, B, were extracted along these horizons and displayed laterally in map view. $\frac{B}{A}$ and $B-A$ were calculated everywhere along the decollement in order to create $\frac{B}{A}$ and $B-A$ attribute maps, in addition to individual A and B attribute maps. The motivation behind a $\frac{B}{A}$ map is to

view lateral changes in AVO slope, sometimes displayed in AVO crossplots, and $B-A$ will show relative changes in Poisson's ratio. The reflector seaward of the trench is within a hydrostatic pressure regime and serves as a baseline AVO response.

Due to the density and velocity decrease of underthrust hemipelagic sediments landward of the trench, the decollement zone reflector was picked as a trough where a mappable horizon exists throughout the frontal prism. The extent of the decollement spans a length beginning at or near the trench and begins to weaken as it nears the crystalline backstop of the wedge that greatly reduces vertical resolution. Approximate extent of a mappable decollement reflector is 10×8 km, and the sub-seafloor reflector spans approximately 10×3 km.

3.4.2 Geometrical Attributes

Seismic geometrical attributes are useful when describing the spatial orientation of seismic events. I used a dip attribute to quantify the dip angle of the seafloor. Here, geometrical attributes help to establish a link between changes in spatial or structural orientation and geologic structure.

Areas along the decollement where pore pressures are hypothesized to be near lithostatic likely have higher fluid content and lower the effective normal stress along the fault plane, and diminish significant stress accumulation within the frontal prism. Alternatively, areas experiencing relatively low pore fluid pressures may increase basal friction, allowing stresses to build within the prism. The proposed net effect is that the frontal prism geometry responds to high pore pressures by decreasing wedge taper and creates a gently dipping seafloor, whereas low pore pressures increase wedge taper and cause steeper dipping seafloor topography. Angle of dip with respect to horizontal was calculated along the seafloor horizon to view how the dip angle varies laterally and compare areas of steep or

gentle seafloor dip to respectively high or low pore pressure values along the decollement.

3.4.3 Reflection Coefficient

The normal incidence reflection coefficient, R_c, is the impedance contrast between two layers and is a function of pressure wave velocity, V_p, and density, ρ, of the upper and lower layers (Equation 3.17). Estimation of this value is beneficial when placing bounds on realistic velocity estimation. Knowledge of ρ_1 and ρ_2 from ODP site 1070 is applied, and estimation of V_{p1} is achieved from careful interval velocity analysis of the data.

$$R_c = \frac{V_{p2}\rho_2 - V_{p1}\rho_1}{V_{p2}\rho_2 + V_{p1}\rho_1} \tag{3.17}$$

In deep water, calculation of the seafloor reflection coefficient, R_{sf}, is done using the relationship between the amplitude of the seafloor arrival and the amplitude of the seafloor multiple arrival in a flat area of the seafloor (Warner, 1990). In a two-layer earth model, the primary reflection amplitude, P, is a source wavelet, $\omega(t)$, is convolved with the seafloor with a given reflection coefficient, R_c, and is recorded at the surface with the addition of random noise, $n(t)$, and spherical divergence of the wavefront as a function of the primary ray path length, r_p (Yilmaz, 2001) (Figure 3.17).

The primary reflection amplitude is given by

$$P(t) = \frac{1}{r_p}\omega(t) * R_{sf}(t) + n(t) \tag{3.18}$$

and the seafloor multiple reflection amplitude is expressed as

$$M(t) = -\frac{1}{r_m}\omega(t) * R_{sf}(t) * R_{sf}(t) + n(t) \tag{3.19}$$

where r_m is the raypath length of the multiple. The amplitude of the multiple is 180° out of phase with the primary amplitude because a phase shift occurs every time the source wavelet is convolved with the ocean-surface reflection coefficient.

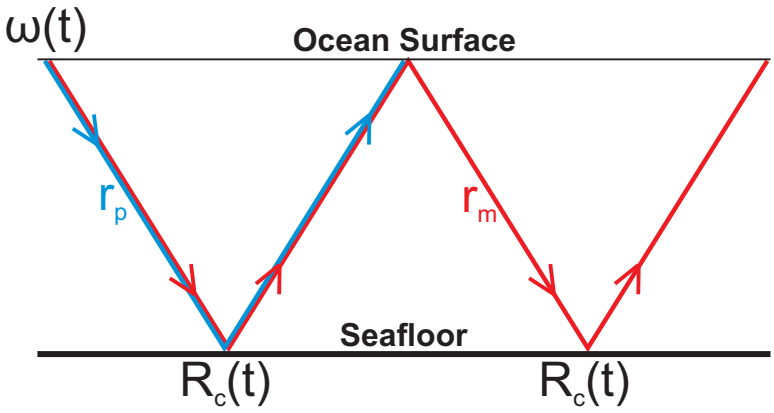

Figure 3.17: Seismic wavefront ray path for primary and first multiple seafloor arrival. The primary and multiple arrivals are used for reflection coefficient estimation.

Transforming Equations 3.18 and 3.19 into the frequency domain yields multiplication instead of convolution, and the ratio of the seafloor multiple to the seafloor primary arrival is expressed as follows:

$$\frac{M(f)}{P(f)} = \frac{-\frac{1}{r_m}\omega(f)R_{sf}(f)R_c(f)}{\frac{1}{r_p}\omega(f)R_{sf}(f)} + n(f) \tag{3.20}$$

$$\frac{M(f)}{P(f)} = -\frac{1}{2}R_{sf}(f) + n(f) \tag{3.21}$$

Transforming back to the time domain and solving for the reflection coefficient we have:

$$R_{sf}(t) = -\frac{2M(t)}{P(t)} + n(t) \tag{3.22}$$

The reflection coefficient is then related to recorded amplitudes by a scaling factor, x, where A_{sf} is the amplitude of the seafloor reflection (Equation 3.23). The amplitude of the decollement, A_d, is scaled by the same factor, x, to calculate the decollement reflection coefficient, R_d (Equation 3.24).

$$x = \frac{A_{sf}}{R_{sf}} \tag{3.23}$$

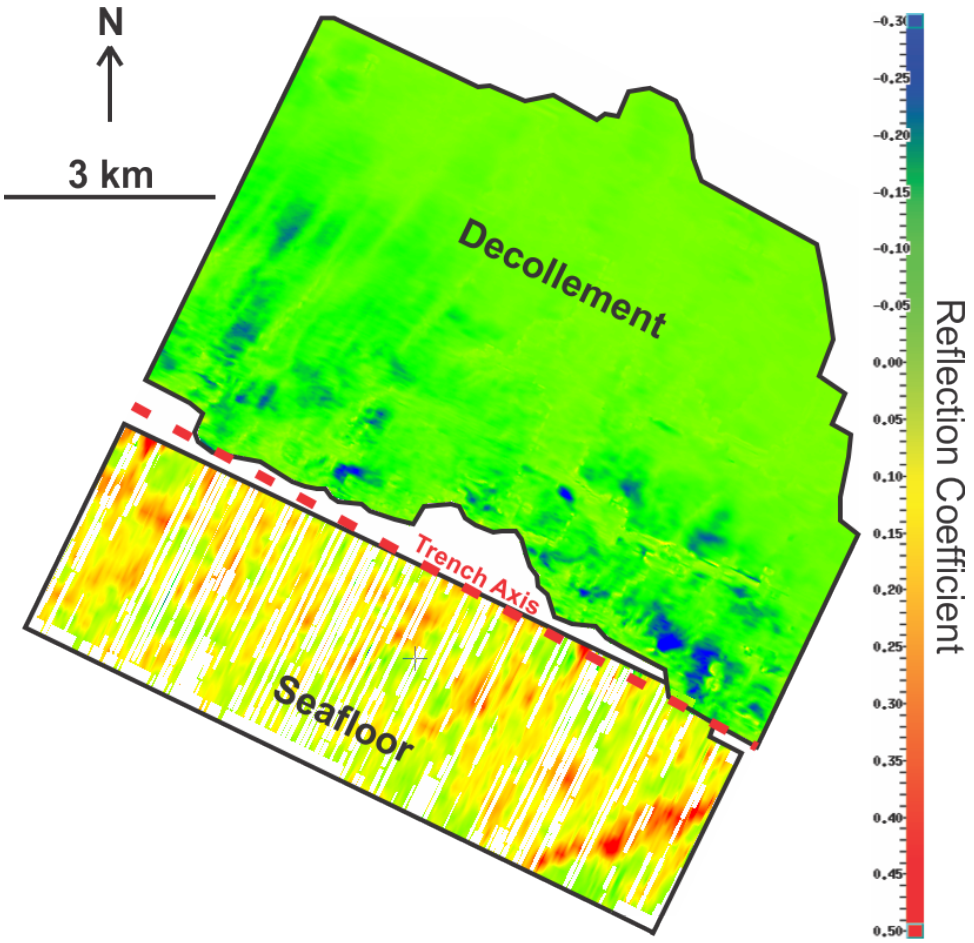

Figure 3.18: Normal incidence reflection coefficient calculation of the seafloor and decollement.

$$R_d = A_d \frac{R_{sf}}{A_{sf}} \tag{3.24}$$

The unmigrated CMP gathers were stacked using a velocity model of 1500 m$\cdot s^{-1}$ everywhere, thus flattening both the seafloor and the seafloor multiple arrivals. Approximately ten traces spanning offsets from 180 m to 300 m were summed together in order to increase the signal-to-noise ratio of the resulting 3D volume. The seafloor and the seafloor multiple seaward of the trench were picked as time horizons where the amplitudes were

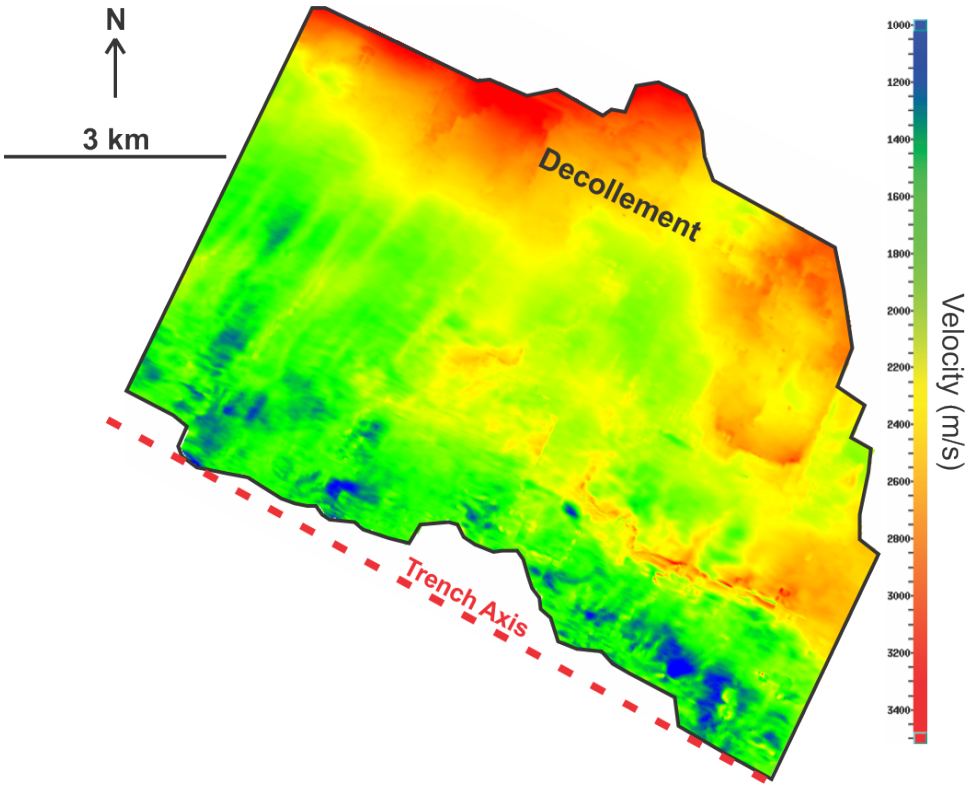

Figure 3.19: V_{p2} calculation along the decollement using the decollement reflection coefficient and assumed values of V_{p1}, ρ_1, and ρ_2.

then extraced for both. The amplitude relationships outlined above were then used to calculate reflection coefficients of the seafloor and the decollement. The scaling factor, x, was averaged over the entire frontal prism, and the decollement amplitudes were scaled with this average value of 250,000 in order to produce a map of the decollement reflection coefficient, R_d (Figure 3.18).

Changes in R_d across the decollement are assumed to be due in large part to changes in velocity of in the decollement, V_{p2}, with fluid content. By knowing R_d, V_{p1}, ρ_1, and ρ_2, V_{p2} was then calculated everywhere along the mapped decollement (Figure 3.19). V_{p1} was extracted along the decollement from the interval velocity volume used to migrate

the CMP gathers. Values for ρ_1 and ρ_2 were taken from ODP leg 170, site 1040, and are the same values used in the one-dimensional block model of Figure 3.9. The maximum and minimum values of V_{p2} observed along the decollement were then used as the upper and lower velocity bounds for the model. Upper and lower bounds are 2.1 $km \cdot s^{-1}$ and 1.5 $km \cdot s^{-1}$, respectively.

From Figure 3.18, the maximum decollement reflection coefficient at presumed areas of near lithostatic pore pressure (≈ -0.20), is in good agreement with the maximum decollement reflection coeffcient derived from the model (≈ -0.22). Similarly, decollement-level velocities in Figure 3.19 are consistent with the maximum and minimum velocities used in AVO modeling presented above. Therefore, the model parameters (V_p and ρ) are valid inputs for our AVO model.

Chapter 4: Observations

4.1 Structure

Within the survey area, oceanic basement is generally unfaulted prior to subduction. Onset of subduction deflects the oceanic crust downward, creating a regime of extensional strain. This causes the formation of stress-relieving normal faults with throws between approximately 75 m and 150 m. Faults trend generally parallel to the strike of the trench axis (Figure 4.1).

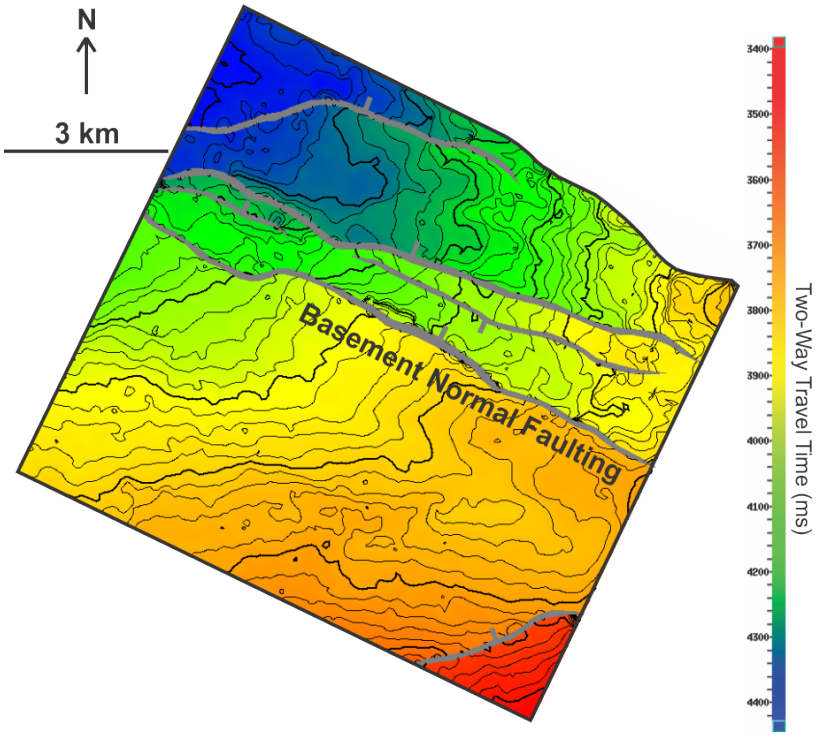

Figure 4.1: Structure map of the interpreted basement horizon. Extensive normal faulting is present landward of the trench axis. Grey polygons indicate fault throw, with ticks indicating the downthrown side of the faults. Contour interval is 20 ms. Note the trend of the normal faulting is parallel to the trench orientation.

Mapping the seafloor structure from the seismic reflection data within the survey area reveals overall greater depths and greater arrival times towards the northwest and shallower depths in the southeast, where warmer colors are shallower in time (Figure 4.2). Seafloor sediment consists of clay and silty sands and exhibits pervasive erosional channels (Kimura et al., 1997). Seaward of the northwest-southeast trending trench axis, the seafloor is slightly shallower towards the southeast than it is in the northwest. This slight structural difference may influence subduction characteristics and overlaying wedge geometry.

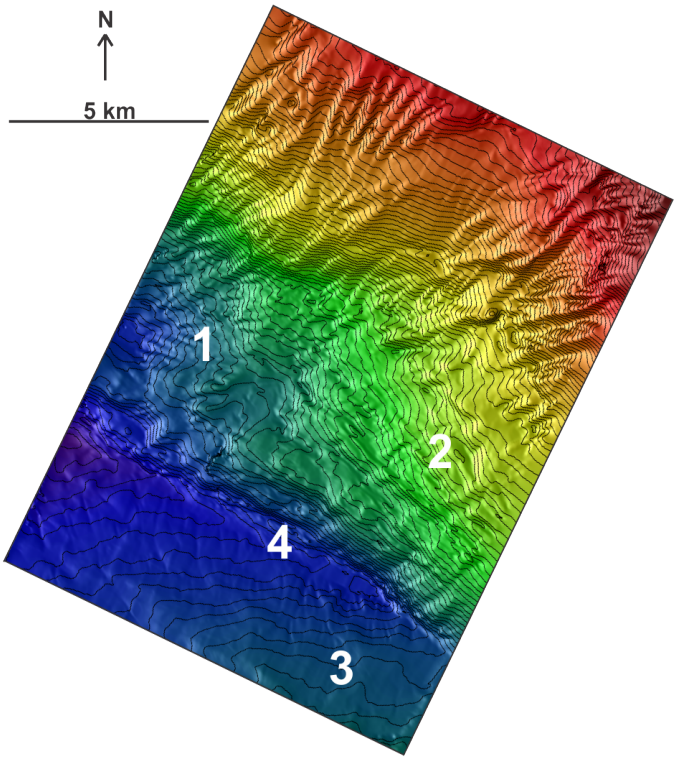

Figure 4.2: Seafloor map of the pre-stack time migrated data area. Warmer colors are earlier in time (shallower). 1) Deeper seafloor topography on the left, 2) shallower seafloor topography on the right, 3) slightly more shallow seafloor seaward of the trench towards the southeast, 4) Mid-America Trench trending northwest-southeast. 20 ms contour interval.

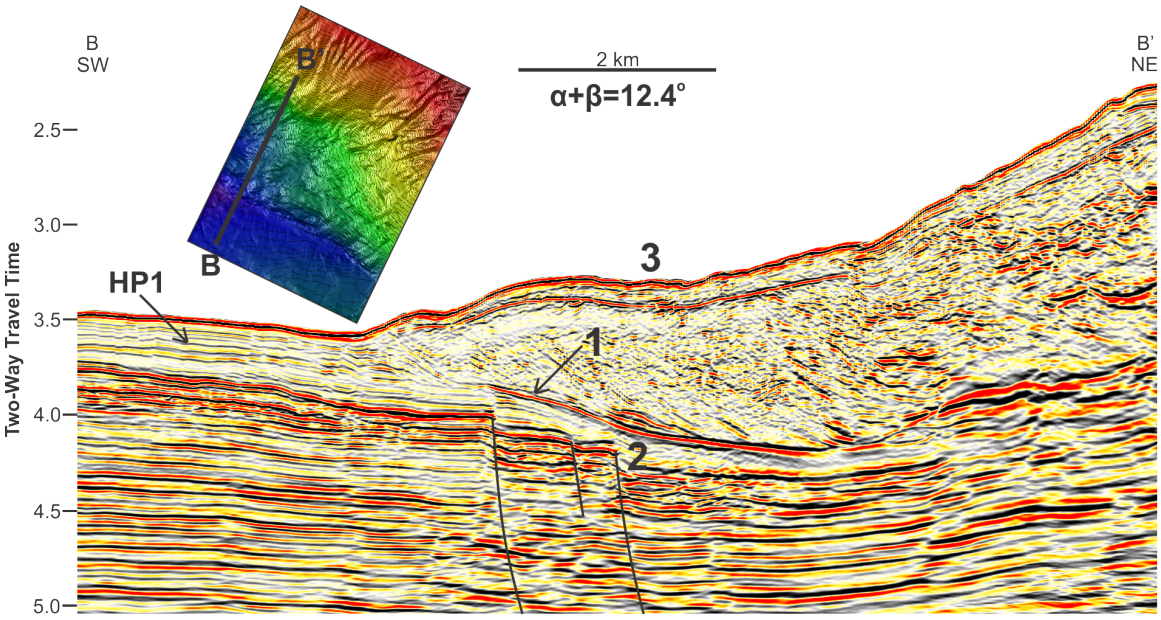

Figure 4.3: Profile B. 1) The negative decollement reflection that becomes weaker near the crystalline backstop; 2) basement normal faulting does not have a pronounced effect on the decollement; and 3) gently dipping seafloor seaward of the crystalline backstop. The reflection event, HP1, was mapped seaward of the trench and provided a baseline AVO response. The taper angle of the frontal prism in profile B is 12.4°.

Seismic profile B in Figure 4.3 spans the entire frontal prism where the negative decollement reflector is clearly imaged until approximately 5 km landward from the trench axis. At this point, the boundary between frontally accreted sediments and proposed crystalline backstop attenuates high frequency events, thereby decreasing the vertical seismic resolution so that the decollement is not imaged as a separate event from the subducting oceanic basement. Here, the decollement reflection is substantially diminished and the high-velocity crystalline backstop distorts the structure of the plate boundary interface between overlying crystalline crust and underlying oceanic crust. In profile B, the decollement is relatively smooth and linear without much distortion from subducting basement normal faults below. Apart from a single basement-level fault seaward of the trench in the

southeast area of the survey (Figure 4.1), basement normal faulting is initiated approximately 1.5 km landward from the trench axis and show a wide range of offsets between approximately 75 m in the northwest to 150 m in the southeast. The offsets in the northwest do not appear to cause substantial displacement of the decollement, and seafloor dip angles are relatively shallow, especially seaward of the crystalline backstop, where the wedge taper angle is 12.4°. Reflection event HP1 (Figure 4.3) is a positive reflection event within the hemipelagic sediments that was mapped throughout the survey area with a high degree of confidence. This reflection event served to provide a baseline AVO response that the decollement AVO response could then be compared against.

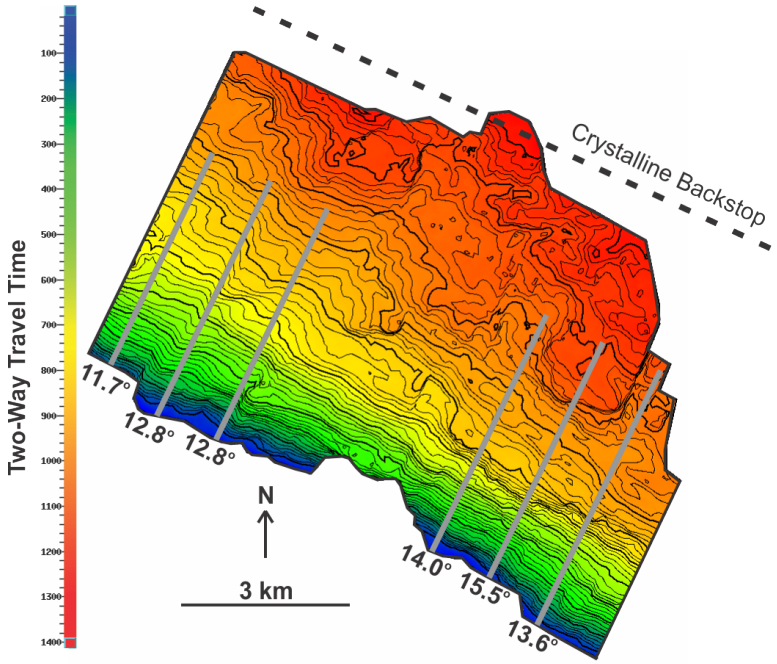

Figure 4.4: Time isopach map of frontal prism thickness. The wedge is thinnest towards the northwest, and thickest towards the southeast. Approximate location of the crystalline backstop is delineated by the dashed line. Frontal prism taper values were calculated along the grey transects.

A time isopach map of thickness between the seafloor and the decollement shows

thinner frontal prism thickness in the northwest and a thicker prism in the southeast (Figure 4.4). Also shown are calculated wedge taper angles, $\alpha + \beta$. The thickest areas of the prism correspond with the largest taper angles of 14.0°, 15.5°, and 13.6° in the southeast part of the survey. The thinnest areas correspond with the smallest taper angles of 11.7°, 12.8°, and 12.8° in the northwest area of the survey. The time isopach map shows that seaward of the crystalline backstop, an overall thickening and increase in taper angle of the wedge occurs towards the southeast.

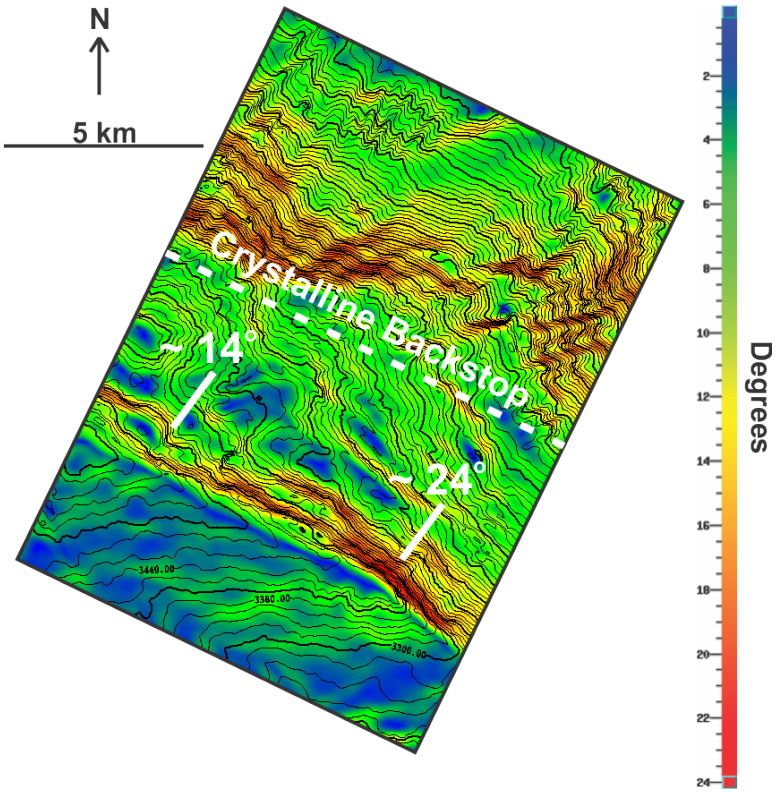

Figure 4.5: Seafloor dip angles ranging from 0° to 24°. Seafloor dip ≈ 14° near the trench are observed in the northwest, and steeper dip angles of ≈ 24° are present towards the southeast. Dip angles become much more pronounced closer to the trench axis.

Seaward of the backstop, steeper seafloor dip angles are observed in the southeast area where the frontal prism is thicker, and gentle dips are present where the prism is

thinnest (Figure 4.5). Only seafloor dip angles seaward of the backstop are considered because this is the landward limit of the accreted frontal prism where prism morphology is influenced on short timescales. The difference in seafloor dip between the northwest and southeast areas is approximately $4^\circ - 5^\circ$ immediately seaward of the backstop, but dip angles become much more extreme near the trench axis. To the northwest, the seafloor dip angle near the trench axis is $\approx 14^\circ$; and to the southeast, the seafloor dip angle is $\approx 24^\circ$. There appears to be a correlation between steep dips, thicker frontal prism, and shallower seafloor arrival times.

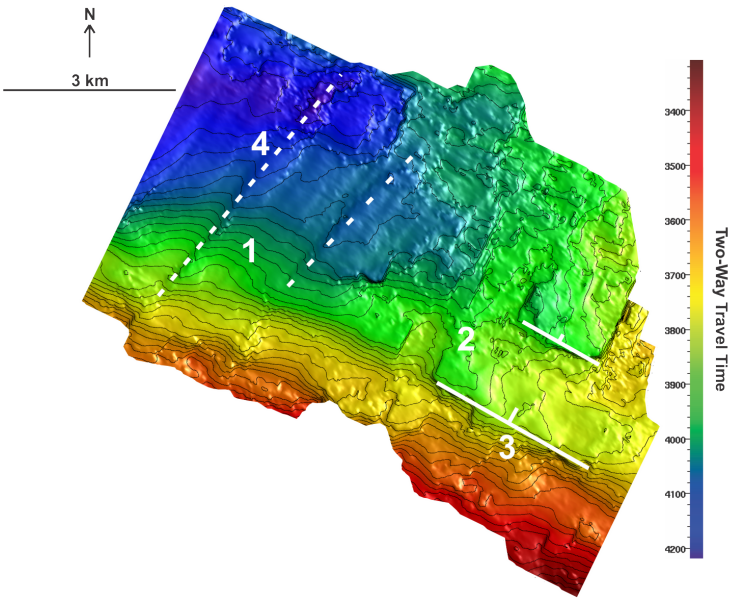

Figure 4.6: 1) Decollement time structure shows a smoother decollement on the left and 2) rougher decollement on the right; 3) basement normal faulting greatly influences decollement structure to the southeast; 4) two trench-perpendicular structural discontinuities are present in the northwest area (dashed lines).

The arrival time of the decollement becomes shallower as it approaches the trench, as shown in the decollement time structure map (Figure 4.6). Cool colors are deeper, and

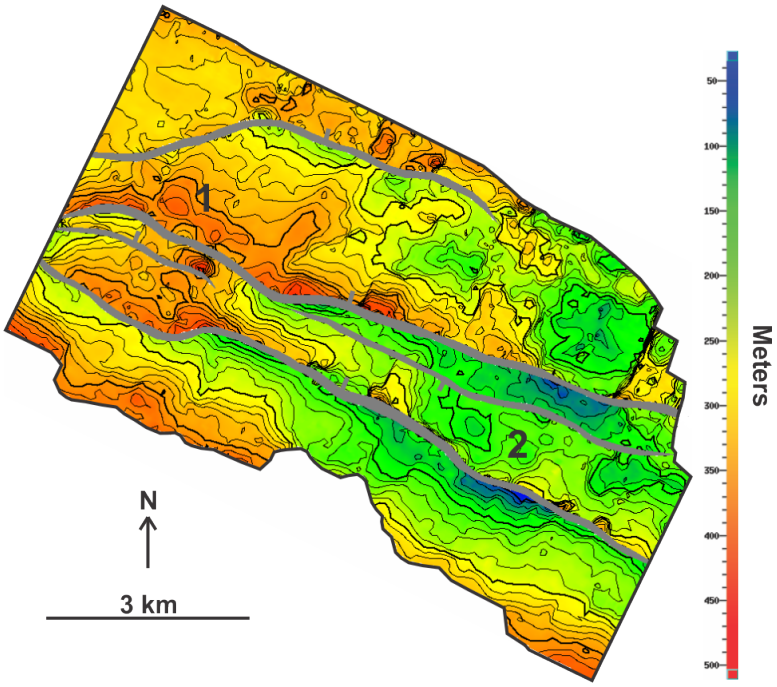

Figure 4.7: Time isopach map of hemipelagic and pelagic sediment thickness between oceanic basement and decollement horizons. 1) Thickest sediment packages are approximately 400 m thick; 2) thinnest areas are between 50 to 150 m thick. Grey lines are basement fault polygons.

warmer colors are shallower. Two dominant basement normal faults influence decollement structure to the southeast. Here, the basement faults have larger offsets and cause significant structural relief in the decollement above the faulting. Decollement structure is smooth in the northwest area of the map and rough in the southeast area of the map. There are two seismic structural discontinuities that trend southwest-northeast in Figure 4.6 and are represented by white dotted lines. These could be fractures that help contain high pore pressure within the decollement.

In order to estimate the thickness of subducting hemipelagic sediments, the decollement and basement horizons were converted to depth with the interval velocity model used for pre-stack Kirchhoff time migration. The approximate depth of the decollement was

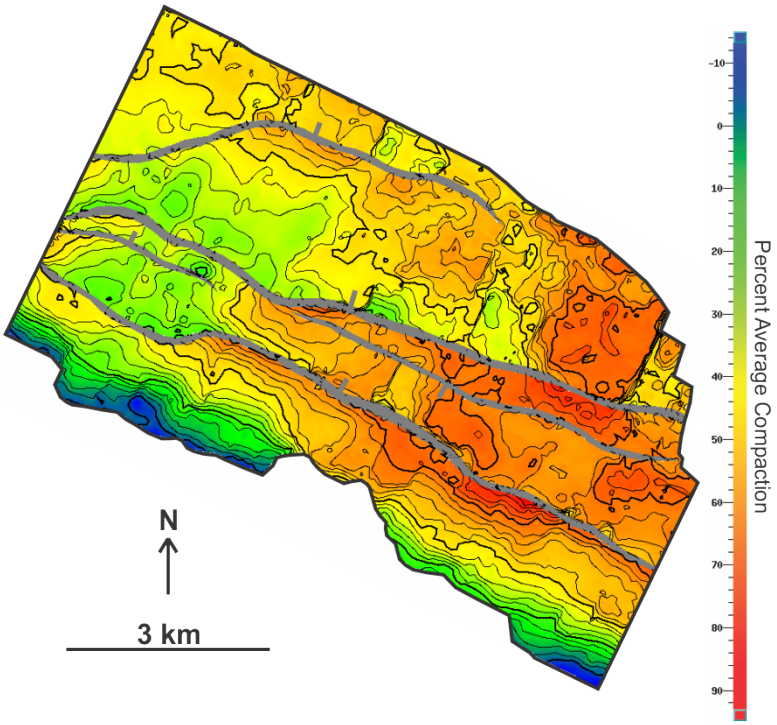

Figure 4.8: Subducted sediment thickness is divided by an average incoming sediment thickness in order to estimate the amount of sediment compaction. Compaction is on the order of 20% towards the northwest and about 60% towards the southeast.

subtracted from the approximate basement depth, resulting in an isopach map representing the vertical thickness of subducting hemipelagic sediments (Figure 4.7). The thickest sediment accumulations are in the northeast area of the survey and correspond with a smooth decollement and relatively low wedge taper angles between 11.7° and 12.8°. The thinnest accumulations reside towards the southeast where the decollement is more discontinuous and the frontal prism exhibits higher taper angles between 13.6° and 15.5°. The percentage of sediment thinning was found by dividing the subducted hemipelagic sediment thickness by an average incoming sediment thickness value of approximately 402 ms in two-way travel time (Figure 4.8). From this, sediments appear to be thinning by as much as 60% in some areas in the southeast, either caused by fluid expulsion and

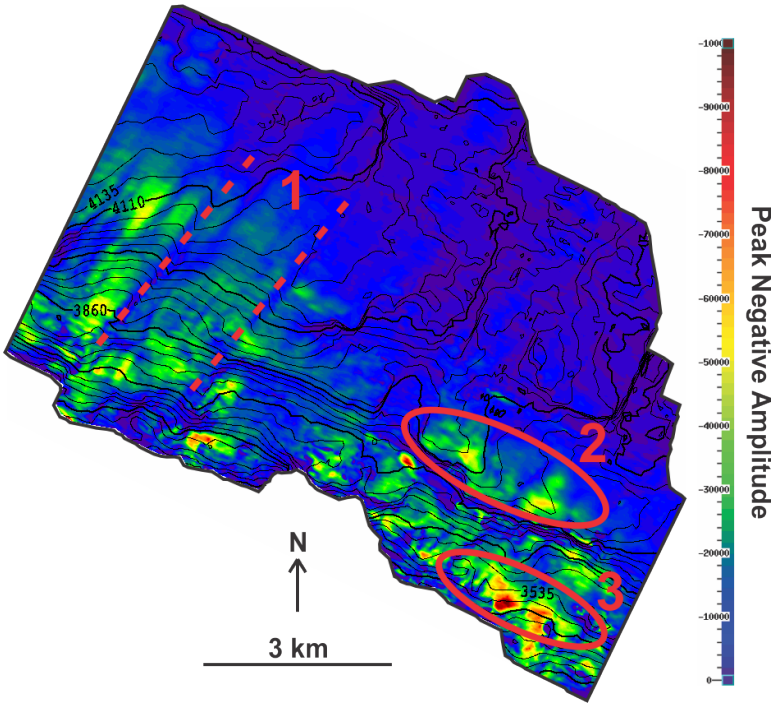

Figure 4.9: A decollement amplitude map shows 1) high, negative amplitude trench-perpendicular features that are bounded by trench-perpendicular structural discontinuities; 2) high amplitudes appear to be isolated on the downthrown side of the basement normal fault expression in the decollement; 3) high amplitude in the southeast near the trench are anomalously high.

compaction, offscraping of incoming sediments near the trench, or both. Even though offscraping is observed proximal to the trench axis, this likely does not account for such low thickness of sediments in the southeast. Therefore, it appears as if the area to the northwest is significantly more undercompacted than sediments in the southeast.

Seismic amplitude extraction along the decollement shows trench-perpendicular, high-amplitude bands in the northwest area of the survey that seem to be separated by the structural discontinuities noted earlier that may laterally contain pore pressures. The decollement exhibits the highest amplitude response near the trench in the southeast area, and high amplitudes are isolated to the downthrown side of the basement normal fault

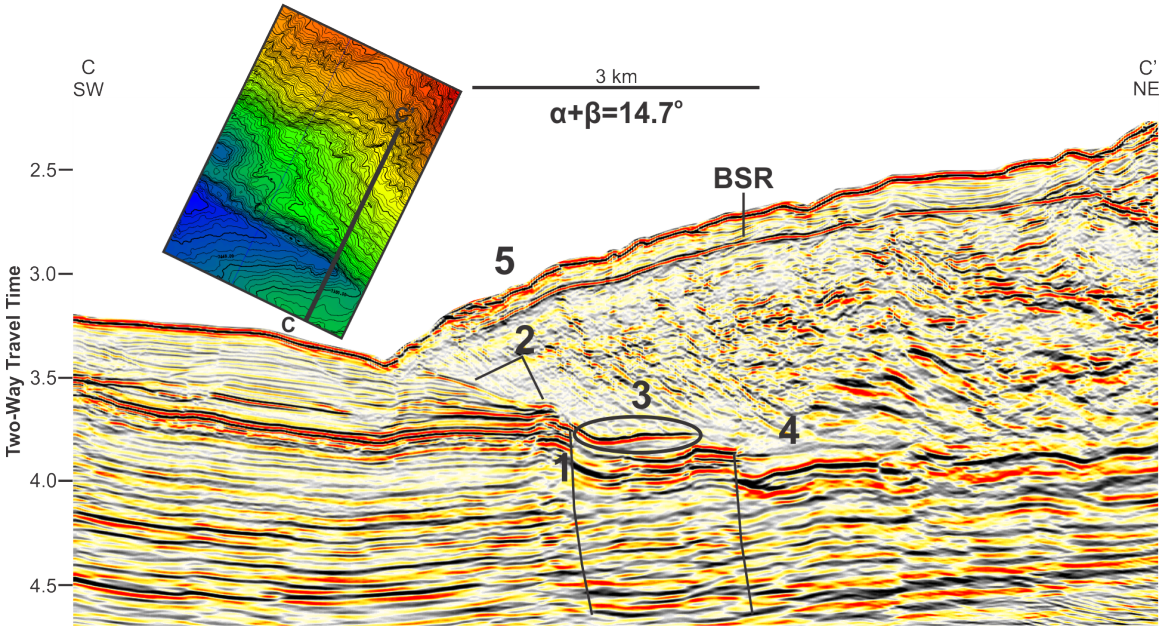

Figure 4.10: Profile C passes through the southeast area of the survey. 1) Basement normal faulting has larger offsets than in the northwest area; 2) decollement reflections are as close as 10 to 20 m from the top of the oceanic basement; 3) high decollement reflection amplitudes are isolated to the down-thrown side of the first fault block; 4) decollement amplitudes diminish past the second basement normal fault; 5) seafloor dip angles become larger in the southeast area of the survey.

(Figure 4.9). The decollement amplitude map initially shows what may be areas of high pore pressure to the northwest, and localized areas of high pore pressure to the southeast near the trench, and low pore pressures distal to the trench in the southeast area. These initial results will be explored in more detail using AVO techniques.

Seismic profile C bisects the frontal prism in the southeast survey area (Figure 4.10). Overall steeper seafloor dips are seen in profile C, along with basement normal faulting with offsets greater than approximately 100 m. The decollement appears to become close enough to the upthrown side of the normal fault to interfere with basement reflections. The vertical resolution of the data at the depth of the decollement in the frontal

prism is approximately 17 m. Therefore, the decollement may be as close as 10 to 20 m from the subducting oceanic basement. Even though the decollement does not appear to be incised by normal faulting, high decollement amplitudes are isolated to the downthrown side of the structurally altered decollement. Landward of the second major basement normal fault, amplitudes become much more diminished and rugose until the decollement extends near the crystalline backstop where the decollement reflection is lost completely (Figure 4.10).

4.2 AVO Attributes

The seismic reflection at the base of the frontal prism exhibits a clear, distinct, reverse polarity reflection event (Figure 4.3(1)) caused by a decrease in acoustic impedance from low-velocity hemipelagic sediments stratigraphically below higher impedance, structurally deformed prism sediments. Generally higher reflection amplitudes exist where the decollement surface is smooth and continuous. Some of the highest amplitude reflection trends are trench-perpendicular features in the northwest part of the survey area (Figure 4.9). Normal incidence reflectivity (A) along the decollement corresponds very well to stacked seismic amplitude response (Figure 4.11). Normal incidence reflectivity trench-perpendicular bands in the northeast as well as isolated reflectivity response along the downthrown normal fault and near the trench all match up well with the stacked seismic amplitude response. Normal incidence reflectivity of the sub-seafloor reflection event within the hemipelagic sediments, HP1, is also shown. This is a positive reflection event, but the absolute magnitude of the reflection is relatively low when compared to high absolute values extracted along the decollement.

The AVO gradient, B, attribute map (Figure 4.12) shows generally high AVO gradients in locations corresponding to high zero incidence reflectivity. The major exception

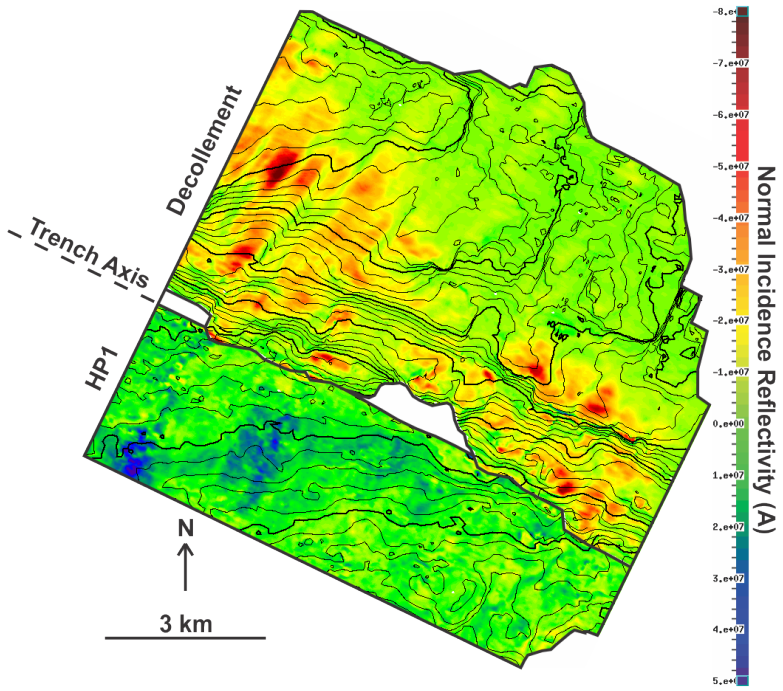

Figure 4.11: Normal incidence reflectivity simulates closely stacked amplitude response. Both the decollement and HP1 reflectivities are shown. HP1 was mapped as a positive reflection event. These reflectivity values are used for the AVO intercept, A.

to this is near the trench in the southeast area of the map. Here, high normal incidence reflectivity and stacked seismic amplitude response are observed. The gradients, however, the gradients in this area appear to be very minimal. Since areas of high fluid content are expected to show both large, negative, normal-incidence reflectivity and large, positive AVO gradients, this area near the trench may have high fluid content but low pore pressures because the AVO gradient in this area is relatively low (Figure 4.12). The AVO gradient landward of the basement normal faulting appears diminished in the southeast half more than in the northwest half of the survey. Similarly, the continuity of the decollement in the southeast half is much less than in the northwest.

The location of high values of $B-A$, i.e., inferred high Poisson's ratio and pore

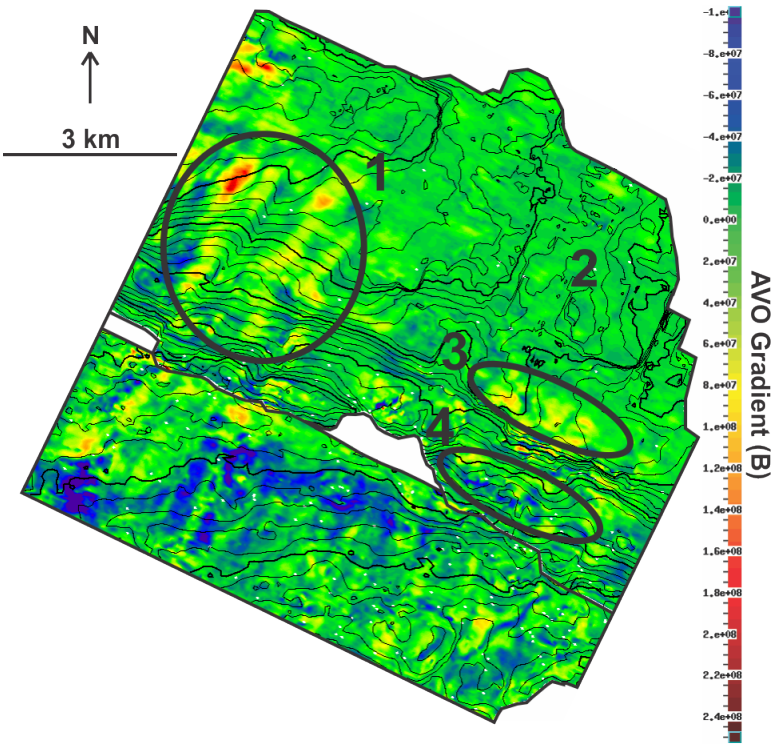

Figure 4.12: The AVO gradient map shows 1) high gradients where the decollement is smoothest and 2) low AVO gradients where the decollement is more discontinuous. 3) AVO gradients are high landward of the first basement normal fault to the southeast and 4) high amplitude reflections near the trench do not show up well on the AVO gradient map.

fluid pressures, (Figure 4.13) generally corresponds to locations of large reflection amplitudes. $B-A$ less than zero are presumed to be outliers, because calibrated modeling suggests positive B and negative A values; thus, only positive values of $B-A$ are included. Reflections with large $B-A$ correspond directly to large amplitude events; however, the $B-A$ map distinctly outlines and discriminates large events more than the amplitude map, as can be seen in the trench near the southeast corner as well as on the downthrown side of the first basement normal fault. Both of these areas have very high stacked amplitude response (Figure 4.9), but the $B-A$ attribute map indicates those areas may have lower pore fluid content than originally anticipated.

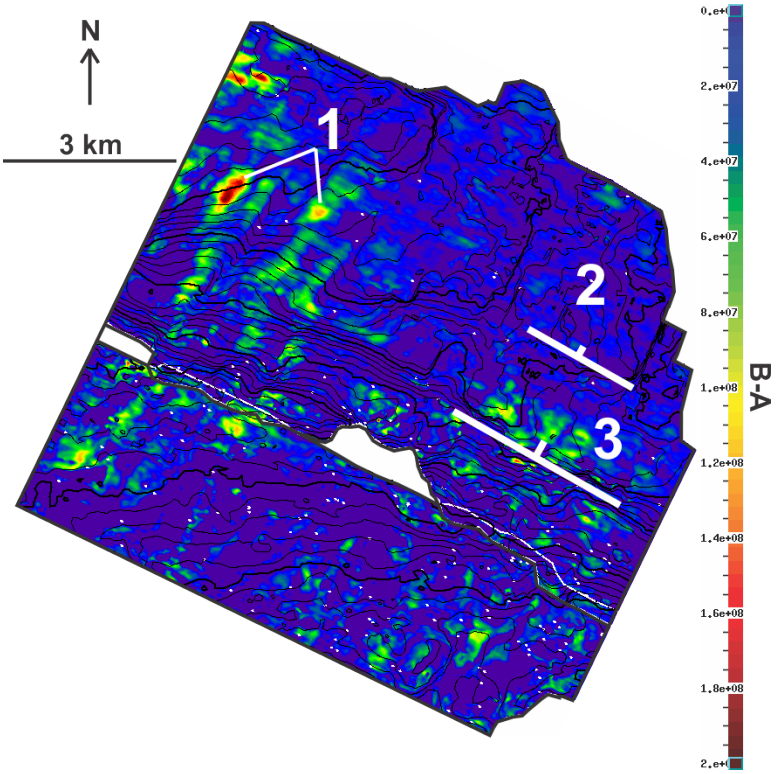

Figure 4.13: B-A is a representation of pore fluid pressure. Warmer colors are interpreted to be areas with higher fluid content and relatively elevated pore fluid pressure within the decollement. The northwest area shows high B-A values (1), whereas the southeast area shows low B-A response (2). Local areas of high B-A within the decollement are present on the downthrown side of basement normal faults (3).

AVO crossplots are commonly used to represent changes in geophysical properties from a normal background trend by plotting the A and B AVO attributes against each other. If there is a strong relationship between A and B, then numerous data points will yield a trend that a best-fit line can be fitted to. The slope of the best-fit line is referred to in this study as the slope of the AVO crossplot. Since a 3D volume of A and B attributes was calculated every 2 ms at every CMP location, it is possible to view the slope of the AVO crossplot in map view by simply dividing $\frac{B}{A}$ at every CMP location along the decollement horizon. The downside to this is that dividing B over A at a single CMP location is essen-

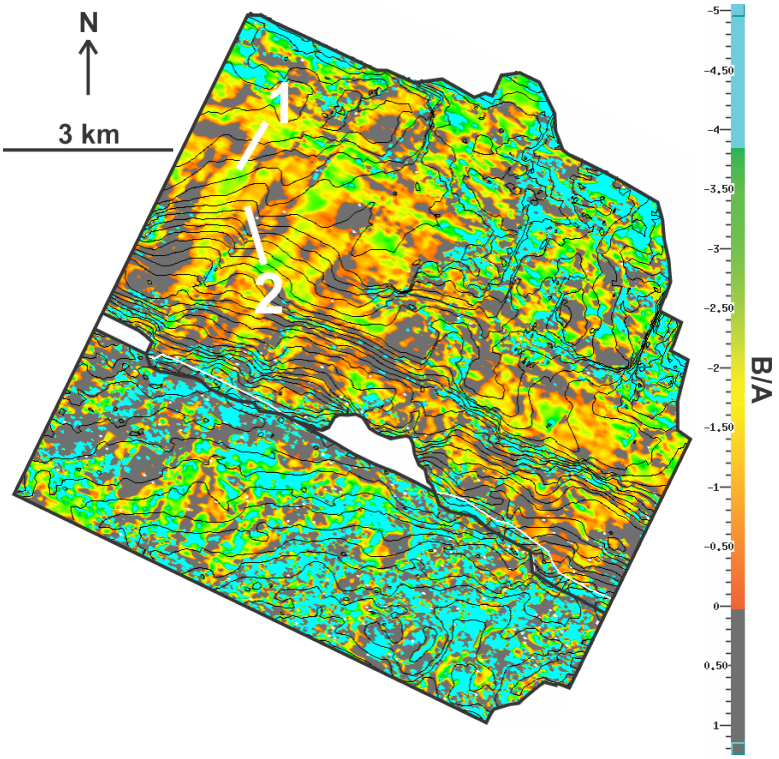

Figure 4.14: 1) $\frac{B}{A}$ outlines similar trends as the B-A map but systematically suggests lower overpressures in areas where B-A shows high overpressures, 2) and shows both high and moderate values associated with overpressures where B-A shows moderate values associated with overpressures. This means that the original model needs to be modified. Blue colors indicate hydrostatic pressure and low fluid content. Warm colors correspond with high pore fluid pressures and high pore fluid content.

tially the slope of the AVO crossplot at one data point. Therefore, the trend is not as robust as the traditional crossplot that plots $\frac{B}{A}$ on one plot within a specified vertical window and horizontal range. The advantage, however, is that approximate AVO crossplot slopes may be viewed laterally over broad areas. Lateral changes in the slope of the AVO crossplot is displayed in Figure 4.14. Similar trench-parallel trends in the northwest area are easy to distinguish, as are the trends on the downthrown side of the first basement normal fault to the southeast.

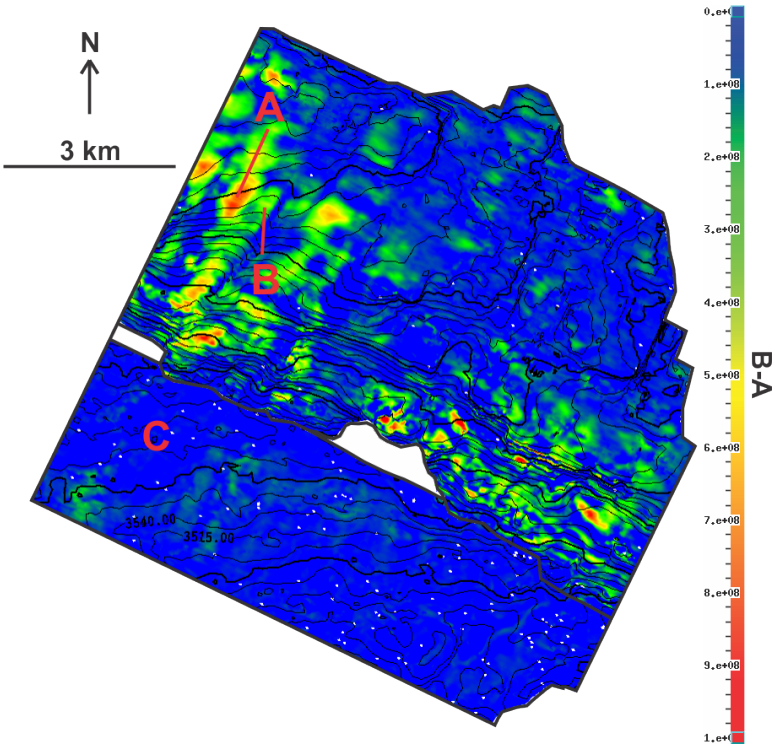

Figure 4.15: Locations of crossplots on B-A map. Location A, high fluid pressure; location B, moderate fluid pressure; location C, high fluid content at hydrostatic pressure.

Initial modeling for calibration of AVO analysis shows that large, negative AVO slope should correspond to large, positive values of $B-A$. Upon further inspection, however, the largest $B-A$ values from the 3D seismic reflection data correspond to areas of only moderate AVO slope (≈ -2.8), and the least negative AVO slopes (≈ -1.7) are equivalent to only moderate $B-A$ values (Figures 4.13 and 4.14). This relationship is seen throughout the decollement and means that the original AVO model does not fully estimate the geophysical properties of the decollement and must be modified. From these key observations comes that idea discussed below: that in order to match modeled the seismically observed results between the $B-A$ and $\frac{B}{A}$ attribute maps, the assumptions of how V_p or V_s changes with increasing pore pressure change. Areas in the slope of the AVO

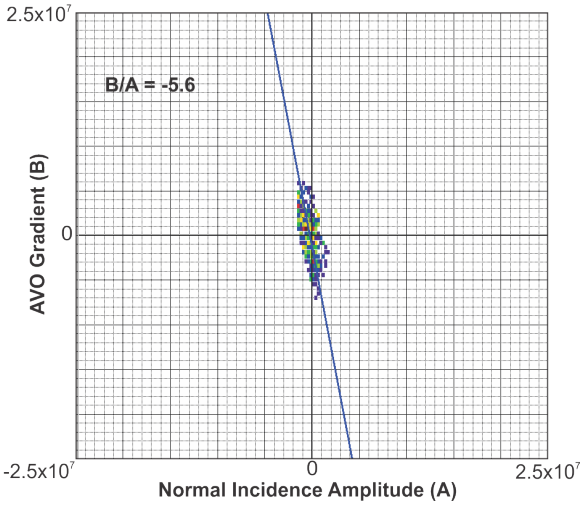

Figure 4.16: Crossplot view of the baseline hydrostataic slope of the AVO crossplot, $\frac{B}{A} \approx -5.6$, calculated at location C in Figure 4.15 from the HP1 reflection. By comparison, modeling shows $\frac{B}{A} \approx -4.58$.

crossplot map that show as grey indicate that there is no significant relationship between B and A. Viewing these areas in the traditional crossplot view will yield a shotgun pattern with no trend. Blue colors indicate hydrostatic values and warmer colors should indicate higher fluid content, yet this may not be true due to discrepancies between the original model and 3D seismic results.

A hydrostatic pressure background trend was sampled along horizon HP1 seaward of the trench axis at location C (Figure 4.15). In crossplot view, hydrostatic $\frac{B}{A} \approx -5.6$ (Figure 4.16). At relatively moderate pore fluid content and pore pressures $\frac{B}{A} \approx -1.7$ (Figure 4.17), as sampled at location B (Figure 4.15). At high pore fluid content and near lithostatic pore fluid pressures, $\frac{B}{A} \approx -2.8$ (Figure 4.18) as sampled at location A in Figure 4.15.

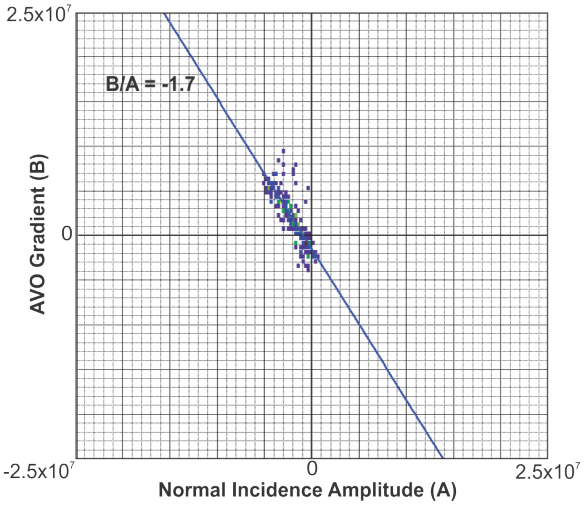

Figure 4.17: Crossplot view of what appears to be a slope of the AVO crossplot corresponding to moderate fluid content, $\frac{B}{A} \approx -1.7$, calculated at location B in Figure 4.15. By comparison, modeling shows $\frac{B}{A} \approx -2.06$.

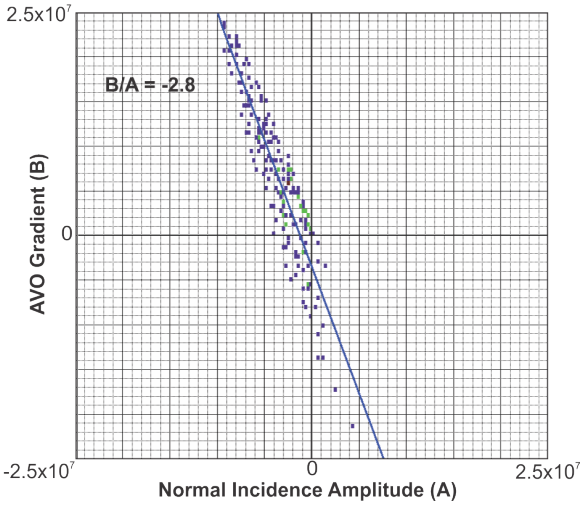

Figure 4.18: Crossplot view of what appears to be a slope of the AVO crossplot corresponding to high fluid content, $\frac{B}{A} \approx -2.8$, calculated at location A in Figure 4.15. By comparison, modeling shows $\frac{B}{A} \approx -2.25$.

The slopes of the A vs. B AVO crossplots are clearly different from what preliminary simulations suggest. Instead of areas with highest fluid content corresponding with the least negative slope of the AVO crossplot, these areas have a moderate AVO crossplot slope that is certainly not the minimum AVO crossplot slope. The minimum AVO crossplot slope instead corresponds with areas of what seem to be moderate pore fluid content. The hydrostatic case with high pore fluid content and low pore fluid pressure seaward of the trench axis has the most negative AVO crossplot slope and behaves as the model predicted.

Chapter 5: Discussion

Preliminary AVO model simulations with experimentally derived velocities of fine- to medium-grained, water-saturated sands (Prasad, 2002), shows that the magnitude of the rate of change of AVO attribute A is larger than the rate of change of attribute B with respect to increases in pore fluid pressure (Figure 5.1). This causes the normal incidence reflection, A, to become more negative faster than the amplitude gradient, B, is becoming positive as pore fluid pressure increases. As a result, the slope of the AVO crossplot at hydrostatic pressures, $\left(\frac{B}{A}\right)_{hyd}$, moderate pressure, $\left(\frac{B}{A}\right)_{mod}$, and lithostatic pressure, $\left(\frac{B}{A}\right)_{lith}$, should be related as $\left(\frac{B}{A}\right)_{hyd} < \left(\frac{B}{A}\right)_{mod} < \left(\frac{B}{A}\right)_{lith}$, meaning that the highest pore pressures correspond with the least negative AVO slope (Figure 3.16).

Crossplots of AVO slopes along the decollement calculated from the CMP gathers show $\left(\frac{B}{A}\right)_{hyd}$ to be in agreement with model results. However, $\left(\frac{B}{A}\right)_{mod}$ is more negative than $\left(\frac{B}{A}\right)_{lith}$ (Figures 4.17 and 4.18), which is in stark contrast with simulated values. In the modeled data, the change in A with respect to λ^* is larger than the change in B with respect to λ^* at high pore fluid content, meaning that A becomes more negative faster than B, causing $\frac{B}{A}$ to become less negative and approach a slope of zero (Figure 3.16). In order for $\frac{B}{A}$ to become more negative at high pore fluid contents and pressures, the gradient of B with respect to λ^* needs to be *greater* than the magnitude of the gradient of A. This may be accomplished in two ways: either the gradient of A is decreased, or the gradient of B is increased. The AVO attribute, A, is primarily a function of the change in V_p and ρ across the interface, and B is largely a function of the change in $\frac{V_p}{V_s}$ across the interface.

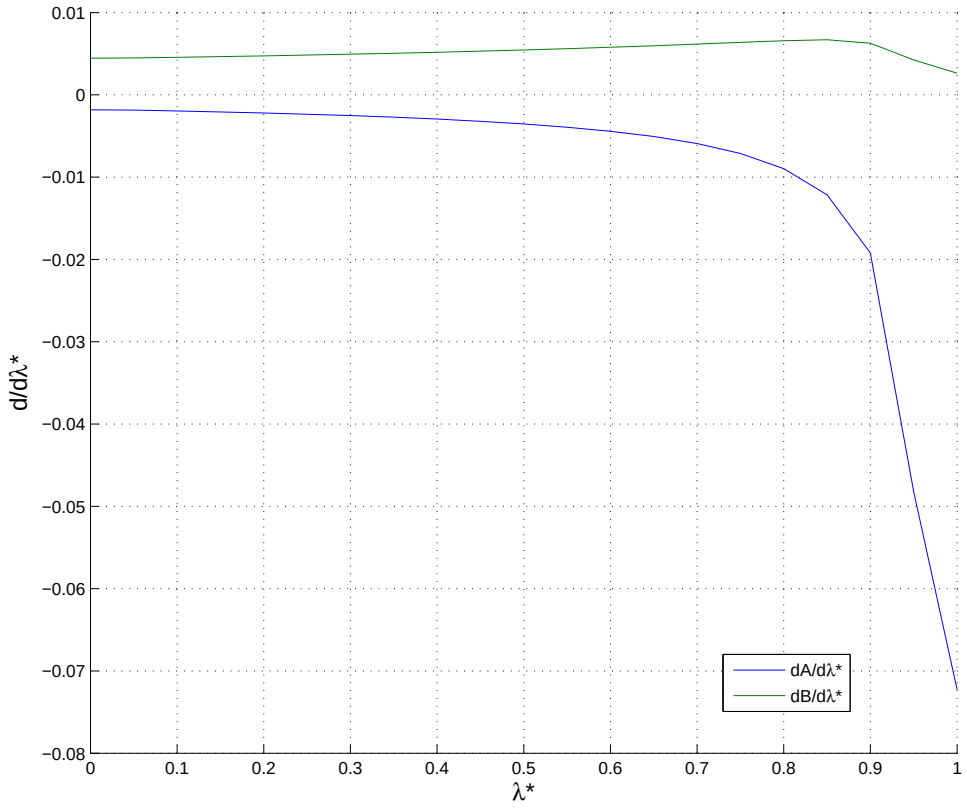

Figure 5.1: The green curve is the derivative of the AVO gradient, B, and the blue curve is the derivative of the AVO A attribute. The derivative of A is always positive and the derivative of B is always negative with increasing pore pressure. However, the absolute value of the derivative of A is larger than the derivative of B during initial modeling using laboratory-derived values of V_p and V_s.

Altering the gradient of B is achieved primarily by changing how V_{s2} responds to changing pore fluid pressures. Making $\frac{B}{A}$ more negative at high pore fluid pressures by changing V_{s2} requires that the shear velocity begin to drop off and trend towards zero at pore fluid pressures significantly less than lithostatic values. Satisfying the aforementioned condition means that the shear velocity will be negligible well before lithostatic pore fluid pressures are reached. In the models, before lithostatic pore pressures are reached, hemipelagic decollement sediments will still be in grain-to-grain contact with one an-

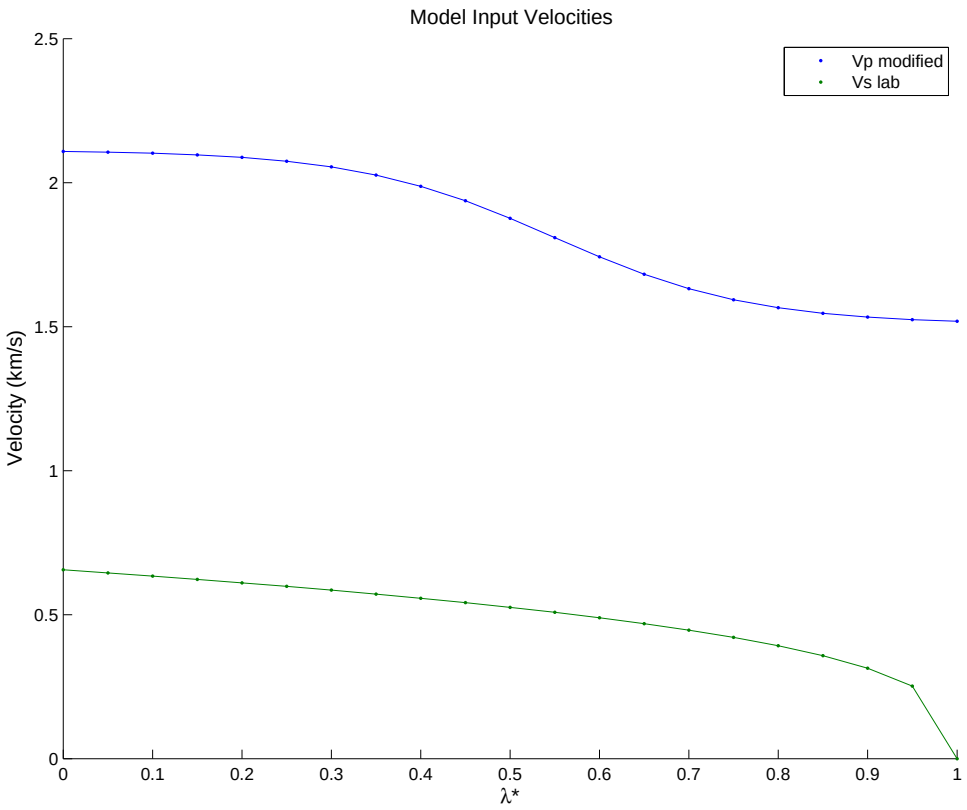

Figure 5.2: Modified velocity functions for V_p and V_s. V_s is the same trend from the Prasad (2002) laboratory data, but the V_p curve has been modified to fit a logistical function that begins to reach a lower limit at high overpressures. Maximum and minimum pressure velocities were derived from reflection coefficient calculation.

other because pore pressures are not high enough to overcome the fracture strength of the decollement, $\sigma_1 + \sigma_3$. Therefore, in the model it is unlikely that V_{s2} goes to zero at pore pressures well below lithostatic.

An alternate scenario to change the gradient of B with respect to λ^* is that the shear velocity within the decollement begins to drop off at lower pore fluid pressures, but decreases at a lower rate until eventually reaching zero near lithostatic pore fluid pressures when sediments loose grain-to-grain contact. Even though mathematically possible, once the shear velocity begins to decrease in a significant manner, it will drop off exponentially

beyond that point because grain-to-grain contacts quickly separate and the shear rigidity of the sediments will drop off markedly. Therefore, changing the model function of $V_s(\lambda^*)$ does not realistically mimic the observed $\frac{B}{A}$ crossplot results.

Prasad (2002) observed that seismic velocities decreased as a power-law function with increasing pore pressure. The experiment was performed on medium- to fine-grained sand samples saturated with water; however, her velocity results do not correctly model AVO response along the decollement, as seen in the misfit between modeled AVO response and response from 3D seismic data. The best way to recreate the AVO response seen in the CMP gathers is to alter the assumptions of how V_{p2} responds to increases of the pore fluid pressure, λ^*.

Altering the change in V_p with increasing pore fluid pressure such that it asymptotically approaches a minimum velocity (Figure 5.2) will cause $\frac{B}{A}$ to become more negative at near lithostatic pore pressures. AVO attribute, A, will slow its rate of change with respect to λ^*, but attribute B will keep changing quickly as high pore pressures are reached (Figure 5.3). The reason for B, i.e., V_s, to keep increasing at a high rate is presumed to be a result of the grain-to-grain behavior of the sediments. No matter the amount or directionality of fractures, the shearing behavior of grain-to-grain contact of the sediments will remain the same, in that even with high fracture density and volume at high pore fluid contents, V_s will still drop off quickly towards zero when there is no contact between grains because the rigidity of the sediments quickly trends towards zero. Conversely, under these same conditions where there is high fracture density and fluid content, V_p may taper towards a minimum velocity, i.e., the propagation velocity of the slurry. At hydrostatic pressure, the sediments are grain-supported, and seismic P-waves and S-waves can freely propagate. At moderate to high pore pressures of $\lambda^* \approx 0.5 - 0.7$, pressure and shear velocities will become lower. At high pore pressures, $\lambda^* > 0.8$, the sediments begin to transition from

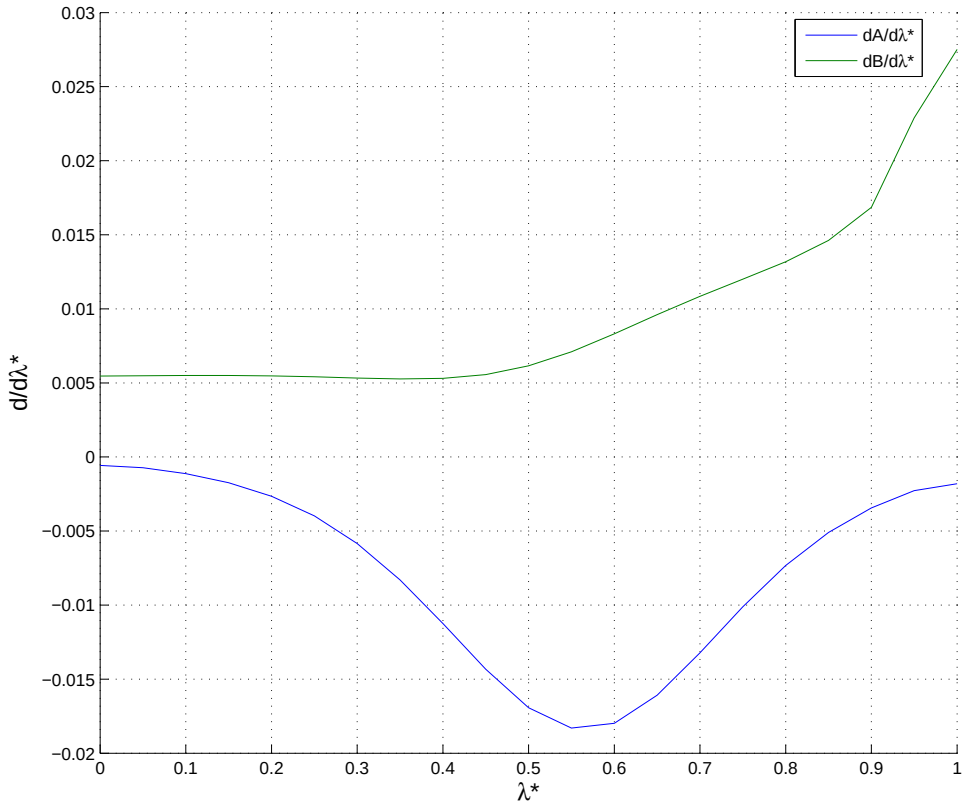

Figure 5.3: The blue curve is the derivative of the AVO A attribute. The rate of change of A decreases at high pore fluid contents and high pore pressures.

grain-supported to fluid-supported, and shear velocities approach zero. During this state, with high fracture density and high fluid content, the sediments become similar to that of a slurry, and P-waves will preferentially propagate at the velocity of the interstitial fluid. As pore pressures reach lithostatic, $\lambda^* \approx 1.0$, V_s is at zero, and V_p decreases towards the velocity of the slurry. However, because V_p was already influenced by the velocity of the fluid, any subsequent increase in pore pressure will have less of an effect on the decrease of V_p. It is for this reason V_p is modeled by a logistic function (Figures 1.5 and 5.2).

Though the rate of change of V_p is less than what was originally modeled, higher values of B-A are still associated with areas of the highest pore fluid pressures as seen

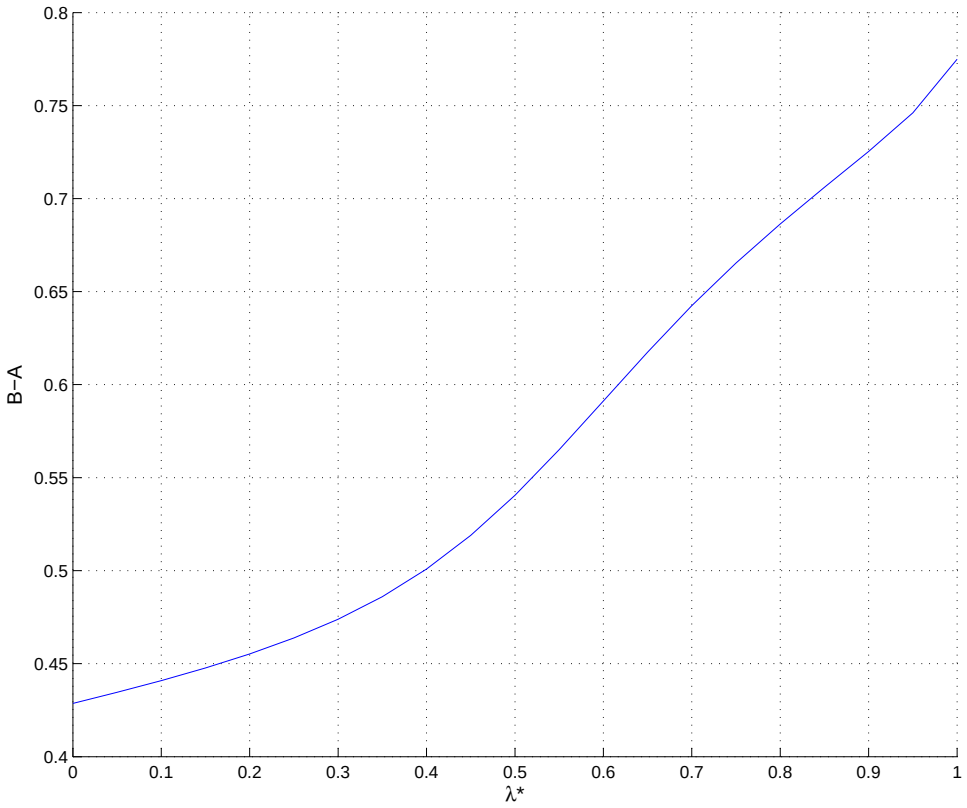

Figure 5.4: The crossplot of λ^* against B-A from modeling with a P-velocity logistic function shows a strong positive correlation with the modified $V_p(\lambda^*)$ relationship, indicating that the B-A attribute is useful for overpressure detection with the modified P-wave velocity function.

in Figure 5.4. Even with a modified $V_p(\lambda*)$ function (Figure 5.2), modeling shows that B-A is still a reasonable attribute for pore fluid pressure estimation (Figure 5.4). Figure 4.13 shows B-A values that correlate to areas of moderate and high overpressure. The areas of high inferred overpressure given by the B-A map correspond to areas of moderate $\frac{B}{A}$ values of ≈ -2.8, and areas of moderate overpressure correspond to areas of high $\frac{B}{A}$ values of ≈ -1.7. These results match well with the modeled results where V_p is modeled as a logistic function (Figure 5.5) and $\frac{B}{A} = -2.246$ at $\lambda^* = 1$. Additionally, the modeled hydrostatic background trend, -4.579, is in close agreement with the background trend

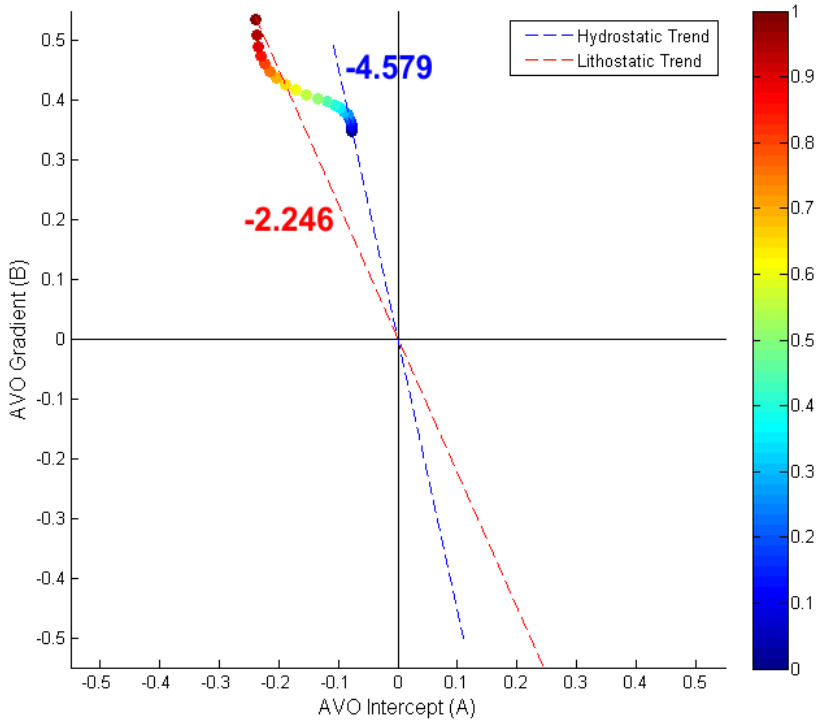

Figure 5.5: Modified $\frac{B}{A}$ crossplot ranging from $\lambda^* = 0 - 1$. The new results show the highest pore fluid content and near lithostatic pore pressures corresponding with moderate AVO crossplot slopes modeled to be -2.246 when $\lambda^* = 1$.

extracted from hemipelagic sediments seaward of the trench axis, -5.8. Using B-A and $\frac{B}{A}$ in conjunction with each other provides a useful tool for overpressure detection within the decollement beneath the frontal prism.

The cause of different V_p behavior is perhaps due to the difficulty of replicating subducted hemipelagic sediments in the lab. Key differences between laboratory measurements and field seismic measurements are that seismically observed frequencies of approximately 35 Hz near the decollement are much lower than experimental frequencies ranging from kHz to MHz, depending on the experimental setup (Prasad, 2002). Further-

more, the lithology of the decollement constitutes very fine-grained hemipelagic sediment that is likely highly brecciated and differs greatly from the unfractured samples used in the lab. Intense fracturing or preferential alignment of fractures and clay particles in the direction of the basal shear stress may factor into different behavior of V_p.

The Costa Rica margin seaward of the trench is dominated by hemipelagic and pelagic clays at ODP sites 1039 (Kimura et al., 1997). This, in conjunction with low shelf sediment supply to the trench, create a setting that is dominated by homogeneous clays. As the homogeneous hemipelagic and pelagic clays are subducted, the absence of sand layers limits dewatering conduits to fractures and the inherent low permeability of the sediments. Areas with low fracture density are likely undercompacted and, due to the lack of sufficient dewatering conduits, are closely tied with areas of high pore fluid pressure. Therefore, areas of high B-A and moderate $\frac{B}{A}$ values are proposed to be not only areas of increased fluid content, but also areas of increased pore fluid pressure as well.

AVO response of high reflection amplitude anomalies on seismic profiles oriented perpendicular to the trench (Figure 4.3 and 4.9) are interpreted to be areas of high pore fluid pressure that are flanked by trench perpendicular seismic discontinuities that may be fractures aiding to contain lateral fluid flow. Figure 4.18 and 4.17 are crossplots taken from data in the northwest area that show near-lithostatic pore pressures at location A and moderate pore fluid pressures at location B, respectively (Figure 4.15). Here, high B-A values are interpreted to correspond to elevated pore fluid content (Figure 4.15). This is consistent with the relatively gentle seafloor dip angles (Figure 4.5), decreased prism thickness, acute taper angles of the overlying frontal prism (Figure 4.4), and under-compacted hemipelagic and pelagic subducted sediments (Figure 4.7). High pore fluid contents may decrease basal friction along the decollement and allow the frontal prism to reach equilibrium after seismic events in accordance with the Wang and Hu (2006) theory

of a dynamic Coulomb wedge.

The southeast survey area exhibits low B-A values (Figure 4.13), low decollement sesimic reflection amplitude (Figure 4.9), and $\frac{B}{A}$ values representing lower pore fluid contents (Figure 4.14). Lower pore pressures in this area are also accompanied by increased taper angles, thickening of the frontal prism, and thin $\approx$ 50 m to 150 m thick subducted sediments. Containment of high pore pressure is also seen on the downthrown side of basement normal faulting in the southeast (Figure 4.14). Here, basement normal faulting is interfering with the decollement reflector and may facilitate release of fluids via induced vertical fractures into the overlying frontal prism. Fluids may also flow trenchward along the decollement until they become close to the basement normal fault, where they are then isolated on the downthrown side. The B-A response of the decollement on the downthrown side of the normal fault in the southeast area of the survey (Figure 4.13), however, is not as high as in the northwest where pressures are higher and are isolated within the decollement. Therefore, even though fluids are isolated in the decollement to the downthrown side of the fault block, the decollement may still be fractured, allowing for upward migration of fluids.

Chapter 6: Conclusions

Explaining pore fluid content and pore fluid pressure conditions within the decollement is important in understanding the initial stages of sediment dewatering underneath the frontal prism. Below are conclusions drawn from the investigation of decollement AVO response.

1. Decollement structure, seismic reflection amplitude, and B-A attribute maps outline two areas of the decollement that show distinct characteristics. The northwest area exhibits a smooth, large reflection amplitude decollement that is unimpeded by subducting basement normal faults, whereas the southeast area shows a rugose and weak reflection amplitude decollement that is heavily inflenced by basement normal faulting.

2. Small wedge taper values of 11.7°, 12.8°, and 12.8° in the northwest are a direct result of high fluid contents and pore fluid pressures that decrease the basal friction and allow for smooth slip along the decollement fault plane.

3. Larger wedge taper values of 14.0°, 15.5°, and 13.6° in the southeast are caused by low pore fluid contents and pressures that increase the basal friction along the decollement and allow for strain accumulation within the frontal prism.

4. The interpretation of B-A and $\frac{B}{A}$ attribute maps along the decollement do not identify the same overpressure localities assuming a power-law $V_p(\lambda^*)$ function. Instead, a $V_p(\lambda^*)$ logistic function, where V_p asymptotically approaches the minimum interstitial fluid velocity, properly links the AVO results observed from both the model

and seismic data. I assert that this updated velocity-pore pressure relationship is primarily caused by increased pore fluids and high pore pressures in undercompacted sediments.

5. In the northwest area of the 3D survey, frontal prism structure, decollement structure, and decollement AVO analysis indicates vertical containment of near lithostatic pore fluid pressures within the decollement. The ability of the frontal prism to act as a pressure seal to the plate boundary interface allows the opportunity for large fluid contents, potentially 46% of incoming sediments, to be carried farther downdip in some areas. This likely influences the depth of the seismogenic zone farther downdip, but is outside the realm of this study.

6. Low decollement pore pressures and fluid content in the southeast of the survey area clearly show the occurrence of higher fluid flux into the overlying frontal prism. Large offset basement normal faults structurally interfere with the decollement interface. I propose that the adjustment of the decollement to this subducting topography allows for the formation of vertical fractures that serve as conduits for upward fluid migration from the decollement and into the overlying frontal prism.

Bibliography

[1] Bangs, N. L., T. H. Shipley, J. C. Moore, and G. F. Moore (1999), Fluid accumulation and channeling along the northern Barbados Ridge decollement thrust, *Journal of Geophysical Research, 104*, 20399–20414.

[2] Bekins, B., A. M. McCaffrey, and S. J. Dreiss (1994), Influence of kinetics on the smectite to illite transition in the Barbados accretionary prism, *Journal of Geophysical Research, 99*, 18147–18158.

[3] Bilek, S. L. and T. Lay (2002), Tsunami earthquakes possibly widespread manifestations of frictional conditional stability, *Geophysical Research Letters, 29*, 1673.

[4] Bilotti, F. and J. H. Shaw (2005), Deep-water Niger Delta fold and thrust belt modeled as a critical-taper wedge: The influence of elevated basal fluid pressure on structural styles, *AAPG Bulletin, 89*, 1475–1491.

[5] Bourgois, J., J. Azema, P. O. Baumgartner, J. Tournon, A. Desmet, and J. Aubouin (1984), The geologic history of the Caribbean-Cocos plate boundary with special reference to the Nicoya ophiolite complex (Costa Rica) and D.S.D.P. results (legs 67 and 84 off Guatemala): A synthesis, *Tectonophysics, 108*, 1–32.

[6] Buchs, D M., R. J. Arculus, P. O. Baumgartner, C. Baumgartner-Mora, and A. Ulianov (2010), Late Cretaceous arc development on the SW margin of the Caribbean Plate: Insights from the Golfito, Costa Rica, and Azuero, Panama, complexes, *Geochemistry Geophysics Geosystems, 11*, 1-35.

[7] Byerlee, J. (1978), Friction of rocks, *Pure and Applied Geophysics, 116*, 615–626.

[8] Castagna, J. P. (1993), AVO analysis–Tutorial and review, in *Offset-Dependent Reflectivity–Theory and Practice of AVO Analysis,* edited by J. Castagna and M. Backus, pp. 3–36, SEG, Tulsa, Oklahoma.

[9] Castagna, J. P., H. W. Swan, and D. J. Foster (1998), Framework for AVO gradient and intercept interpretation, *Geophysics, 63*, 948–956.

[10] Cloos, M. (1984), Landward-dipping reflectors in accretionary wedges: Active dewatering conduits?, *Geology, 12*, 512–522.

[11] Davis, D., J. Suppe, and A. Dahlen (1983), Mechanics of fold-and-thrust belts and accretionary wedges, *Journal of Geophysical Research, 88*, 1153–1172.

[12] Davis, E. E. and H. W. Villinger (2006), Transient formation fluid pressures and temperatures in the Costa Rica forearc prism and subducting oceanic basement: CORK monitoring at ODP Sites 1253 and 1255, *Earth and Planetary Science Letters, 245*, 232–244.

[13] DeMets, C., R. G. Gordon, D. F. Argus, and S. Stein (1994), Effect of recent revisions to the geomagnetic reversal time scale on estimates of current plate motions, *Geophysical Research Letters, 71*, 2191–2194.

[14] Dix, C. H. (1955), Seismic velocities from surface measurements, *Geophysics, 20*, 68–86.

[15] Ide, S., A. Baltay, and G. C. Beroza (2011), Shallow dynamic overshoot and energetic deep rupture in the 2011 M_w 9.0 Tohoku-Oki earthquake, *Science, 332*, 1426–1429.

[16] Hubbert, M. K. and W. W. Rubey (1959), Role of fluid pressure in mechanics of overthrust faulting, *Bulletin of the Geological Society of America, 70*, 115–166.

[17] Kimura, G., E. Silver, P. Blum, et al. (1997), *Proc. ODP. Init. Repts.,*, 170: College Station, TX (Ocean Drilling Program).

[18] Koren, Z. and I. Ravve (2006), Constrained Dix inversion, *Geophysics, 71*, 113–130.

[19] Lissinna, B., K. Hoernle, and P. van den Bogaard (2002), Northern migration of arc volcanism in western Panama: Evidence for subduction erosion?. *Eos Trans. AGU, 83*, 1463–1464.

[20] Mavko G., T. Mukerji, and J. Dvorkin (2009), Seismic wave propagation, in *The Rock Physics Handbook: Tools for Seismic Analysis of Porous Media,* pp. 81–168, Cambridge University Press, New York, New York.

[21] McIntosh, K. D. and M. K. Sen (2000), Geophysical evidence for dewatering and deformation processes in the ODP Leg 170 area offshore Costa Rica, *Earth and Planetary Science Letters, 178*, 125–138.

[22] Meschede, M., P. Zweigel, W. Frisch, and D. Völker (1999), Mélange formation by subduction erosion: the case of the Osa mélange in southern Costa Rica, *Terra Nova, 11*, 141–148.

[23] Morell, K. D., E. Kirby, D. M. Fisher, and M. van Soest (2012), Geomorphic and exhumational response of the Central American Volcanic Arc to Cocos Ridge subduction, *Journal of Geophysical Research, 117*, 1–23.

[24] Ostrander, W. J. (1984), Plane-wave reflection coefficients for gas sands at nonnormal angles of incidence, *Geophysics, 49*, 1637–1648.

[25] Prasad, M. (2002), Acoustic measurements in unconsolidated sands at low effective pressure and overpressure detection, *Geophysics, 67*, 405–412.

[26] Ranero, C. R. and R. von Huene (2000), Subduction erosion along the Middle America convergent margin, *Nature, 404*, 748–752.

[27] Resnick, J. R. (1993), Seismic data processing for AVO and AVA analysis, in *Offset-Dependent Reflectivity–Theory and Practice of AVO Analysis,* edited by J. Castagna and M. Backus, pp. 175–189, SEG, Tulsa, Oklahoma.

[28] Rutherford, S. R. and R. H. Williams (1989), Amplitude-versus-offset variations in gas sands, *Geophysics, 54*, 680–688.

[29] Saffer, D. M., E. A. Silver, A. T. Fisher, H. Tobin, and K. Moran (2000), Inferred pore pressures at the Costa Rica subduction zone: implications for dewatering processes, *Earth and Planetary Science Letters, 177*, 193–207.

[30] Saffer, D. M. and C. Marone (2003), Comparison of smectite- and illite-rich gouge frictional properties: application to the updip limit of the seismogenic zone along subduction megathrusts, *Earth and Planetary Science Letters, 215*, 219–235.

[31] Saffer, D. M. and H. J. Tobin (2011), Hydrogeology and mechanics of subduction zone forearcs: Fluid flow and pore pressure, *Annual Review of Earth and Planetary Sciences, 39*, 157–186.

[32] Sato, M. and T. Ishikawa, N. Ujihara, S. Yoshida, M. Fujita, M. Mochizuki, A. Asada (2011), Displacement above the hypocenter of the 2011 Tohoku-Oki earthquake, *Science, 332*, 1395.

[33] Scholz, C. H. (1998), Earthquakes and friction laws, *Nature, 391*, 37–42.

[34] Shipley, T. H., K. D. McIntosh, E. A. Silver, and P. L. Stoffa (1992), Three-dimensional seismic imaging of the Costa Rica Accretionary Prism: Structural diversity in a small

volume of the lower slope, *Journal of Geophysical Research, 92*, 4439–4459.

[35] Shuey, R. T. (1985), A simplification of the Zoeppritz equations, *Geophysics, 50*, 609–614.

[36] Teichert, B. M. A., M. R. Torres, G. Bohrmann, and A. Eisenhauer (2005), Fluid sources, fluid pathways and diagenetic reactions across an accretionary prism revealed by Sr and B geochemistry, *Earth and Planetary Science Letters, 239*, 106–121.

[37] Tobin, H., P. Vannucchi., and M. Meschede (2001), Structure, inferred mechanical properties, and implications for fluid transport in the décollement zone, Costa Rica convergent margin, *Geology, 29*, 907–910.

[38] von Huene, R., J. Miller, D. Taylor, and D. Blackman (1985b), A study of geophysical data along the Deep Sea Drilling Project active margin transect off Guatemala, in *Initial reports of the Deep Sea Drilling Project,* vol. 84 edited by R. von Huene and J. Aubouin, p. 967, U.S. Government Printing Office, Washington, D.C.

[39] von Huene, R. (1986), To accrete or not accrete, that is the question, *Geologische Rundschau, 75*, 1–15.

[40] von Huene, R., C. R. Ranero, and W. Weinrebe (2000), Quaternary convergent margin tectonics of Costa Rica, segmentation of the Cocos Plate, and Central American volcanism, *Tectonics, 19*, 314–334.

[41] von Huene, R., C. R. Ranero, and P. Vannucchi (2004), Generic model of subduction erosion, *Geology, 32*, 913–916.

[42] Yilmaz, Ö. (2001), Migration, in *Seismic Data Analysis: Processing, Inversion, and Interpretation of Seismic Data,* vol. 1 edited by S. Doherty, pp. 463–654, SEG, Tulsa,

Oklahoma.

[43] Wang, K. and Y. Hu (2006), Accretionary prisms in the subduction earthquake cycles: The theory of dynamic coulomb wedge, *Journal of Geophysical Research, 111*, B06410, doi: 10.1029/2005JB004094.

[44] Wang, K., Y. Hu, R. von Huene, and N. Kukowski (2010), Interplate earthquakes as a driver of shallow subduction erosion, *Geology, 38*, 431–434.

[45] Warner, M. (1990), Absolute reflection coefficients from deep seismic reflections, *Tectonophysics, 173*, 15–23.

[46] Zoeppritz, K. (1919), Erdbebenwellen VIII B, Über reflexion und durchgang seismischer Wellen durch Unstetigkeitsflachen, *Gottinger Nachr. 1*, 66–84.